Additive Manufacturing 91 (2024) 104332

Contents lists available at ScienceDirect

Additive Manufacturing

journal homepage: www.elsevier.com/locate/addma

Enhancing the fatigue resistance of high and medium entropy alloys by manufacturing-driven microstructural developments

You Sub Kim [a], Mao-Yuan Luo [b], Dunji Yu [c], Ke An [c], Yan Chen [c], In-Hwan Oh [d], Eunjoo Shin [d], Wanchuck Woo [d], Hobyung Chae [d], Young-Sang Na [e], Peter K. Liaw [f], Jayant Jain [g], Jun Hyun Han [a], E-Wen Huang [b,*], Soo Yeol Lee [a,**]

[a] Department of Materials Science and Engineering, Chungnam National University, Daejeon 34134, Republic of Korea
[b] Department of Materials Science and Engineering, National Yang Ming Chiao Tung University, Hsinchu 30013, Taiwan
[c] Neutron Scattering Division, Oak Ridge National Laboratory, Oak Ridge, TN 37831, United States
[d] Neutron Science Division, Korea Atomic Energy Research Institute, Daejeon 34057, Republic of Korea
[e] Extreme Materials Institute, Korea Institute of Materials Science, Changwon 51508, Republic of Korea
[f] Department of Materials Science and Engineering, University of Tennessee, Knoxville, TN 37996, United States
[g] Department of Material Science and Engineering, Indian Institute of Technology Delhi, New Delhi 110016, India

ARTICLE INFO

Keywords:
Low-cycle fatigue
Stacking-fault energy
Manufacturing process
CoCrFeNiMn
CoCrNi

ABSTRACT

Excellent fatigue performance is essential for broader applications of structural materials. In the present work, we report a microstructural design that improves fatigue resistance for high and medium-entropy alloys fabricated by direct energy deposition and hot-rolling processes. Specifically, we discover that the concurrent evolution of microstructures with fine-structure, including stacking faults, nano-twins and hexagonal-close-packed (HCP) structures, leads to zig-zag fracture that hinders crack propagation under cyclic loadings. These multiple characteristic microstructures improve fatigue resistance, which are attributed to the combination of low effective stacking fault energy and a high capacity for strain energy density. Anisotropic microstructural evolution is driven by the correlation between partial dislocations and the resolved shear stresses depending on the crystallographic orientation relationship. Consequently, stacking faults and nano-twins form prominently in the {111} grains under tension and in the {200} grains under compression. The current work provides an effective method to design advanced alloys for high fatigue resistance through microstructural tuning that controls the stacking fault energy combined by manufacturing processes.

1. Introduction

In our daily life, automobiles, ships, aerospace, bridges, and buildings consistently experience fatigue (i.e., repeated cyclic deformation) below their yield strengths. Meanwhile, they encounter fatigue phenomena above the yield strength due to unforeseen physical accidents and unpredictable natural disasters, such as earthquakes [1,2]. These cyclic-deformation features cause significant deterioration of mechanical properties, ultimately leading to fatigue failure and catastrophic accidents. To prevent accidents and to extend materials life, there is a demand for structural materials with high mechanical strengths and fatigue-endurance limits. However, conventional alloy systems have bottleneck in improving strength, ductility, and toughness together without any trade-off effects. To breakthrough these challenges, innovative alloy systems, such as high- and medium-entropy alloys, have been developed [3–10]. The distinctive characteristics of entropy alloys, such as sluggish diffusion kinetics [11,12], cocktail effects [12,13], severe lattice distortion [14–16], multicomponent precipitates [17–20], short-range ordering [21–24], and tunable stacking fault energy (SFE) [25–28], facilitate an enhanced strength-ductility combination in terms of tensile property. In addition, several mechanisms to improve the fatigue endurance of entropy alloys have been achieved by controlling the grain size [29,30], designing the microstructure [31], optimizing the manufacturing process [32], and yielding precipitates evolution [20]. According to recent reports, high-entropy alloys (HEAs) have a longer fatigue life than conventional metallic alloys [33,34]. Moreover, the

* Corresponding author.
** Correspondence to: Materials Science and Engineering, Chungnam National University, Daejeon 34134, Republic of Korea.
E-mail addresses: ewenhuang@nycu.edu.tw (E.-W. Huang), sylee2012@cnu.ac.kr (S.Y. Lee).

https://doi.org/10.1016/j.addma.2024.104332
Received 7 June 2024; Received in revised form 22 July 2024; Accepted 31 July 2024
Available online 3 August 2024

CoCrNi medium-entropy alloy (MEA) exhibits a higher cyclic strength, lower inelastic strain, and longer fatigue life compared to the CoCrFeMnNi alloy [35]. More recently, the development of the additive manufacturing (AM) technology, which provides several advantages such as short lead time, design flexibility, and minimal material waste, has enabled the fabrication of advanced alloys with improved mechanical properties [36–38]. During the AM process, small melt powders experience rapid heating and cooling rates, resulting in the development of distinct microstructures characterized by high dislocation density, directional grains, and sub-grains [39–41]. This unique microstructure in AM alloys contributes to improving the tensile properties [40–43]. Collectively, the combination of high- and medium-entropy alloys with the AM techniques, i.e., AM-entropy alloys, is expected to have excellent tensile performance [7,36,44,45]. Numerous studies have been conducted to elucidate the strengthening mechanisms of AM-entropy alloys, focusing on grain structures, dislocation, precipitates, nano-twins, and phase transformation [7,8,46–49]. However, despite their advantages in tensile properties, AM-alloys exhibit significant weaknesses in fatigue properties [38,50]. The AM microstructure, obtained directly from the melt pool with a complex thermal history, contains inhomogeneous microstructure, lack of fusion, porosity, and various defects [38,51–53]. These microstructural characteristics result in inferior fatigue resistance [50,54–56] and constrain the widespread adoption of AM technology in industrial applications. Some studies suggest methods such as porosity control [57] and post heat treatment [50,58] to improve the fatigue properties of AM alloys. However, these studies solely focus on AM-conventional alloys. Therefore, there is limited knowledge on the fatigue properties of AM-entropy alloys, especially for direct energy deposition (DED) process. Furthermore, in contrast to monotonic tension, cyclic deformation involves both tension and compression, exhibiting anisotropy deformation mechanisms. Monitoring real-time microstructural evolution during cyclic deformation is crucial for understanding the fatigue mechanisms. To answer these issues, we systematically investigate the differences in fatigue mechanisms between HEAs and MEAs fabricated by hot rolling and DED processes through in-situ neutron diffraction combined with multiscale microstructure analysis. The crucial point of this study is the discovery of a DED CoCrNi MEA with great fatigue performance compared to other additive manufactured alloys, and comparable to or even better than those fabricated by conventionally-processed traditional alloys, even without any post-processing and/or post heat-treatment. Furthermore, the DED CoCrNi MEA exhibits a great fatigue lifetime similar to hot-rolled CoCrNi MEA without significant degradation. We find that these results are driven from the unique microstructural characteristics generated by the DED process. The key is to tailor the microstructural design by tuning the effective stacking-fault energy according to the manufacturing system. The current work paves the way for a practical approach to developing advanced AM alloys with high fatigue resistance for widespread application in industry.

2. Experimental procedures

2.1. Sample manufacturing

The cast-wrought CoCrNi and CoCrFeNiMn alloys are fabricated by an induction furnace under an argon gas atmosphere. The ingots are homogenized at 1200 ℃ for 24 h and then hot-rolled at 620℃ until the thickness reduction reached 65 %. The hot-rolled CoCrNi and CoCrFeNiMn are annealed at 1000℃ for 1 h for recrystallization. The AM CoCrNi and CoCrFeNiMn alloys are fabricated by the DED process under an argon gas atmosphere, and DED powders are made by gas atomization. The manufacturing process conditions are described as follows: a fiber laser with a power ranging from 380 to 400 W, a scan speed of 14 mm/s, a spot size of 0.8 ~ 1.2 mm, a powder size of 40 ~ 150 μm, a powder feed rate of 0.042 g/sec, a layer thickness of 250 μm, and a hatch spacing of 400 μm. In the present work, the CoCrNi and CoCrFeNiMn manufactured by hot-rolling followed by annealing for recrystallization are denoted as the HR CoCrNi and HR CoCrFeNiMn, respectively. The CoCrNi and CoCrFeNiMn fabricated by AM-DED are referred to as the DED CoCrNi and DED CoCrFeNiMn, respectively. The chemical compositions of the studied alloys and DED powders are analyzed using inductively coupled plasma (ICP) are shown in Table S1. We conduct energy dispersive spectroscopy (EDS) analysis for DED alloys to verify the uniformity of elemental distribution (Fig. S1). The DED samples are machined out after AM process, and surface is polished to a roughness level equivalent to 600 grit. The geometric dimension for the fatigue and tensile samples used in the in-situ neutron experiments is a cylindrical shape with a diameter of 6.35 mm and a gauge length of 13 mm and 30 mm, respectively. For the lab scale ex-situ experiments, the fatigue samples are cylindrical type with a diameter of 8 mm and a gauge length of 9 mm, while the tensile samples are plate-shaped with a width of 6 mm, a thickness of 3 mm, and a gauge length of 12.5 mm. Mechanical loading direction and building direction of DED samples are perpendicular, while the loading direction and rolling direction of HR samples are parallel.

2.2. Microstructure characterization

All samples for the microstructure analysis are prepared in initial states and after fatigue tests. The surfaces of the samples are mechanically polished to achieve a mirror-finished surface using 6, 3, and 1 μm diamond suspensions. Subsequently, the mirror-finished samples for electron backscatter diffraction (EBSD) and electron channeling contrast imaging (ECCI) analyses are subjected to electrical polishing using a 35 wt% nitric acid solution at 5 V for the CoCrNi alloys and a solution consisting of 5 vol% perchloric acid (with a 60 wt% concentrated) and 95 vol% methanol at 60 V for the CoCrFeNiMn alloys. The transmission electron microscope (TEM) samples are prepared by z-polishing using a solution consisting of 10 vol% perchloric acid (with a 70 wt% concentrated) and 90 vol% methanol at 20 V and −50℃ for the CoCrFeNiMn and a solution consisting of 10 vol% perchloric acid (with a 70 wt% concentrated), 20 vol% glycerol, and 70 vol% methanol solution at 17 V and −30℃ for the CoCrNi.

2.3. In-situ neutron-diffraction measurements

In-situ neutron-diffraction experiments are conducted under tensile loading and tension-compression cycling strain (low cycle fatigue), respectively, using an MTS load-frame on the VULCAN Engineering Materials diffractometer at the Spallation Neutron Source (SNS) of the Oak Ridge National Laboratory (ORNL) [59]. We conduct tensile experiments under a continuous loading mode with a strain rate of 5×10^{-5}/s. A high strain amplitude of ± 1 % is selected for low-cycle-fatigue (LCF) experiments. Neutron data are collected in a continuous loading mode with a strain rate of ~ 5.6×10^{-6}/s at specific cycles. During other fatigue cycles, where neutron data is not acquired, fatigue tests are performed at a strain rate of 5×10^{-3}/s. Diffraction patterns are simultaneously monitored using two detector banks. Bank 1 and 2 have scattering vectors parallel and perpendicular to the loading axis, respectively. The collected neutron data are chopped and analyzed using the VULCAN Data Reduction and Interactive Visualization software (VDRIVE) [59]. The lattice strain of each {hkl} grain is calculated by $\varepsilon_{hkl} = \left(d_{hkl} - d^0_{hkl}\right)/d^0_{hkl}$, where d^0_{hkl} is the reference interplanar d-spacing in a stress-free condition, and d_{hkl} is the interplanar d-spacing under loading [60].

2.4. Four-circle neutron diffractometer

Four-circle neutron diffractometer (FCD) experiments are conducted at the High-flux Advanced Neutron Application Reactor (HANARO) of the Korea Atomic Energy Research Institute (KAERI) in Korea [61]. The

neutron monochromator of FCD is a single slab of a mosaic Ge (311) crystal and provides a wavelength of 1.31Å. We use the θ/2θ scan method to measure the FCC diffraction peaks of {111}, {200}, and {220} while keeping the number of monitor counters constant. The sample is rotated per 5° in both phi (ϕ, 0° ~ 360°) and chi (χ, 0° ~ 90°) directions. Phi represents the rotation direction of the sample, and chi indicates the rotation direction of the goniometer. We remove the background data from the {hkl} diffraction peak data for accurate texture analysis.

2.5. Convolutional multiple whole profile (CMWP) analysis

The Convolutional Multiple Whole Profile (CMWP) [62] method is used for fitting the convoluted diffraction profiles [63–65]. The dynamic evolution of the dislocation density, stacking faults, and twin probability analyzed by the CMWP-fitting procedures are based on the variation of the peak-shape and peak-width broadening of the diffraction profiles. The formation probability of the stacking faults and twinning are directly determined based on the shifts and breadths of the sum of symmetrical and asymmetrical Lorentzian function-based sub-profiles, given by fifth-order polynomials of the planar fault density [64,66]. The type of sub-profiles follows the specific selection rule for the *hkl* indices of the Bragg reflections [64].

3. Results

3.1. Initial microstructures

EBSD and ECCI analyses results are presented in Fig. 1. The HR CoCrNi has an equiaxed grain structure (Fig. 1a) with Σ3-type annealing twins (Fig. 1i). It exhibits low kernel averaged misorientation (KAM) values (Fig. 1e). The HR CoCrFeNiMn reveals an equiaxed microstructure. And yet, the grain size is relatively non-uniform (Fig. 1c). The low KAM value and the development of annealing twins are similar to the HR CoCrNi (Fig. 1g and 1k). The grain size distribution of HR CoCrNi and HR CoCrFeNiMn are 4 ~ 65 μm and 4 ~ 99 μm, respectively. The DED alloys show distinct grain morphologies and misorientation from the HR alloys. The DED CoCrNi has a columnar grain structure, which is elongated along the building direction. However, the small grains at the melt pool boundary grow in the transverse direction (Fig. 1b). Furthermore, the DED CoCrNi has a higher KAM value, compared to the HR CoCrNi (Fig. 1f). It means that significant residual stress exists within the DED CoCrNi. Similar to DED CoCrNi, columnar grains are generated in the DED CoCrFeNiMn. Fine grains are observed at the melt pool boundary (Fig. 1d) in DED CoCrFeNiMn, and it has the highest KAM value (Fig. 1h) compared to DED CoCrNi. The grain size distribution of DED CoCrNi and DED CoCrFeNiMn are 12 ~ 209 μm and 10 ~ 130 μm, respectively. A solidification cell structure is observed in both DED CoCrNi and DED CoCrFeNiMn due to the fast-cooling rate (Fig. 1j). DED CoCrFeNiMn exhibits a slightly larger solidification cell structure compared to DED CoCrNi. The size of the cell structure is approximately 2 ~ 4 μm for DED CoCrNi and 3 ~ 5 μm for DED CoCrFeNiMn. It is evident that substantial amounts of micro- and nano-porosity developed in DED alloys (Fig. 1j and 1l). These pore type is keyhole porosity, and they are randomly distributed regardless of cell-structure boundary and interior.

3.2. Mechanical properties

Fig. 2a and Table S2 show the mechanical properties from the tensile experiments. The DED alloys typically exhibit a higher yield strength

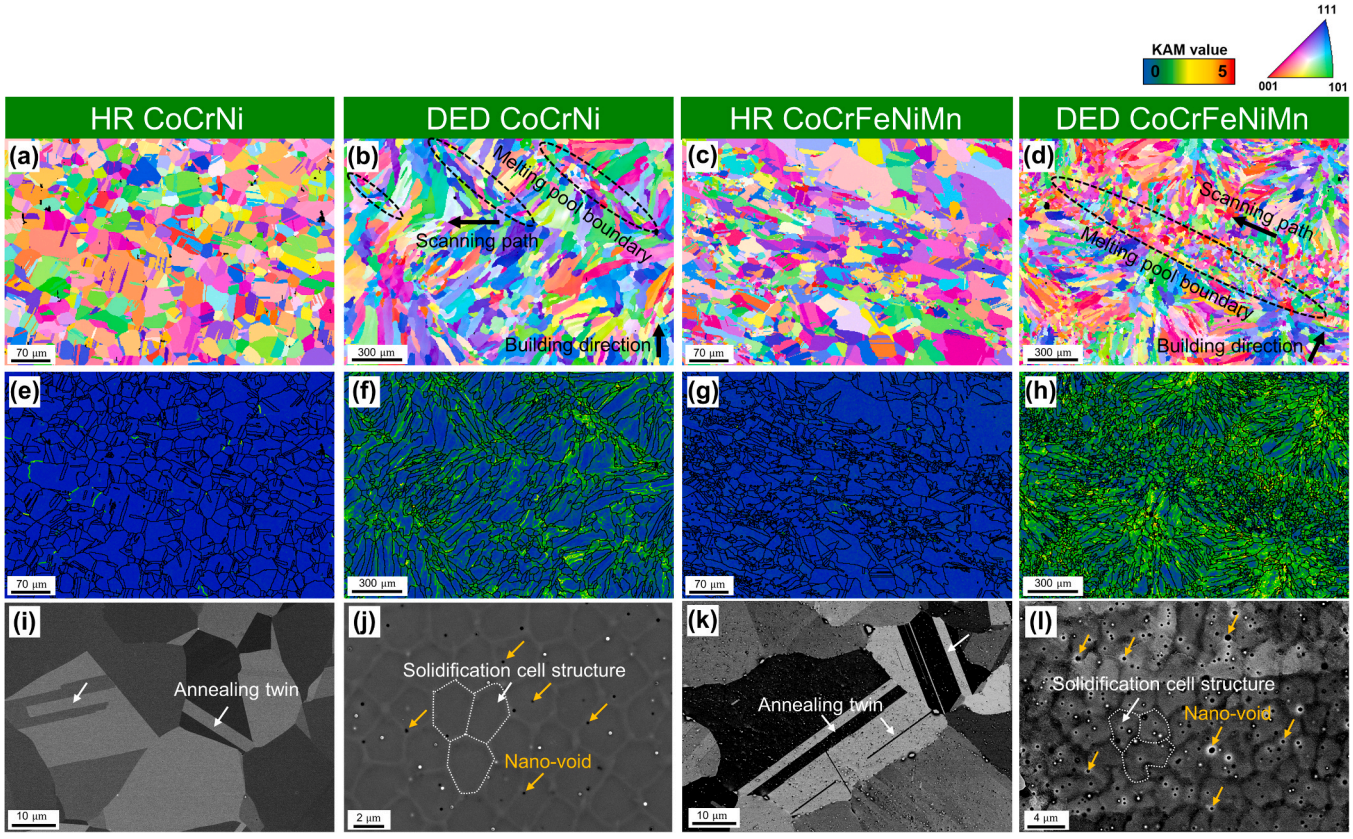

Fig. 1. Initial microstructure: inverse pole figure (IPF) map of (a) HR CoCrNi, (b) DED CoCrNi, (c) HR CoCrFeNiMn, and (d) DED CoCrFeNiMn; kernel averaged misorientation (KAM) maps of (e) HR CoCrNi, (f) DED CoCrNi, (g) HR CoCrFeNiMn, and (h) DED CoCrFeNiMn; electron channeling contrast images (ECCI) of (i) HR CoCrNi, (j) DED CoCrNi, (k) HR CoCrFeNiMn, and (l) DED CoCrFeNiMn. Note that all of microstructure-analysis are conducted on cross-section perpendicular to the loading direction of cylindrical sample.

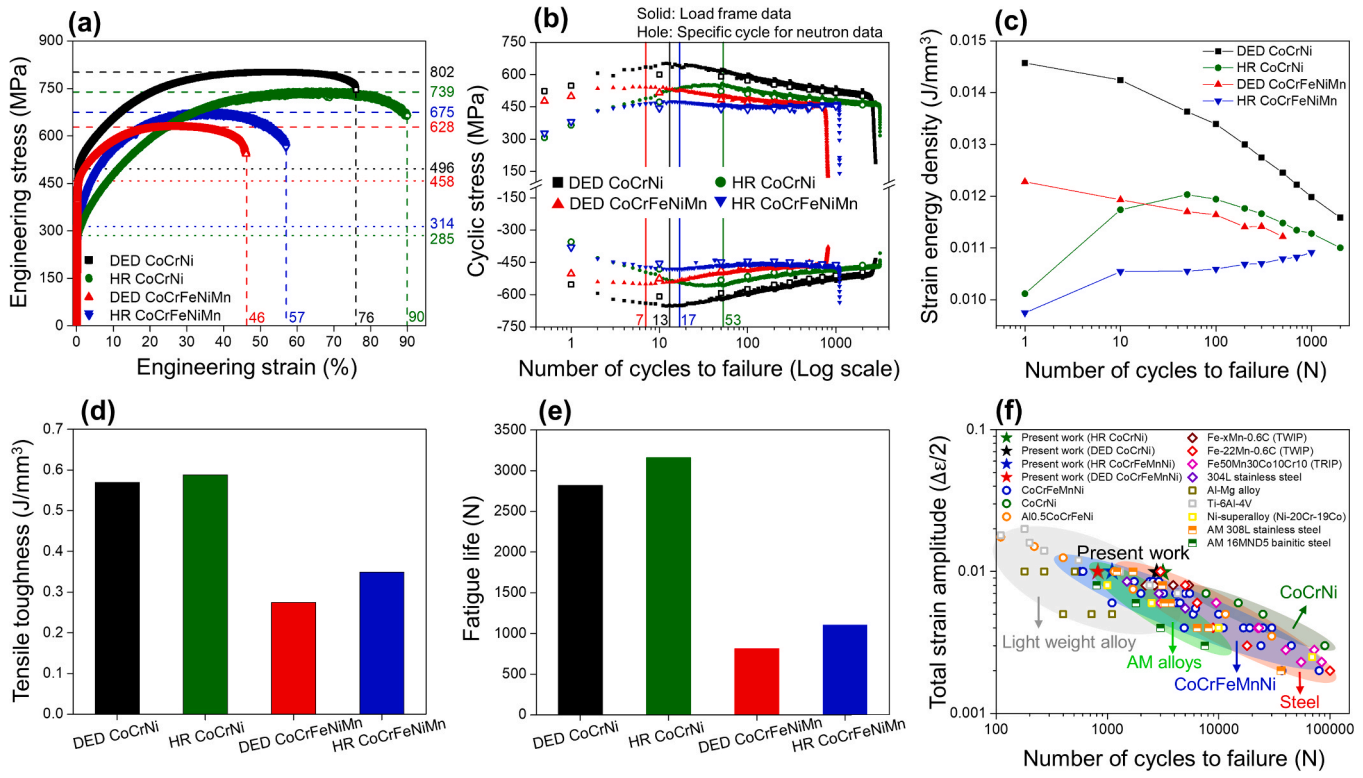

Fig. 2. Tensile and low-cycle-fatigue properties: (a) engineering stress-strain curves, (b) cyclic-stress evolution at total strain of ± 1 % vs. number of cycles to failure, (c) plastic strain energy density vs. number of cycles to failure, (d) comparison of the tensile toughness, (e) comparison of fatigue life, and (f) comparison of the fatigue life with other reported alloys [20,29,30,32,33,35,68–78].

(YS), compared to the HR alloys, but they have a lower ductility. Additionally, the uniform elongations of DED alloys are shorter than those of the HR alloys. The DED CoCrNi has an excellent combination of YS (496 MPa) and ultimate tensile strength (UTS) (802 MPa) with excellent ductility at 76 %. The HR CoCrNi has the highest ductility at 90 %, but its YS and UTS are 285 MPa and 739 MPa, respectively, which are lower than those of the DED CoCrNi. On the other hand, the CoCrFeNiMn alloys demonstrate inferior tensile properties, compared to the CoCrNi alloys. We calculate the tensile toughness by integrating the area under the strain-stress curve from tensile experiment. In terms of tensile toughness, the HR and DED CoCrNi alloys exhibit approximately twice as large as the HR and DED CoCrFeNiMn alloys. In addition, the HR CoCrNi has a slightly higher tensile toughness than the DED CoCrNi (Fig. 2d).

The cyclic-stress response is typically associated with the underlying deformation mechanisms and affect the fatigue life. Its behavior as a function of fatigue cycles is presented in Fig. 2b. Note that fatigue life is determined based on the point at which the samples are fractured and we also perform lab scale ex-situ experiments to double check the fatigue life (Fig. S2). The initial cyclic stresses for the DED CoCrNi are the highest, followed by those for the DED CoCrFeNiMn, HR CoCrFeNiMn, and HR CoCrNi (Fig. 2b), which agree well with the order in the YS of the tensile tests (Fig. 2a). The transition from cyclic hardening to softening in the DED alloys occurs earlier than in the HR alloys. The order of this transition is described as follows: the DED CoCrFeNiMn at the 7th cycle, DED CoCrNi at the 13th cycle, HR CoCrFeNiMn at the 17th cycle, and HR CoCrNi at the 53rd cycle. The DED CoCrNi consistently exhibits the highest level of peak stress during fatigue. However, in the case of the HR CoCrNi, despite having the lowest initial peak stress among the studied alloys, continuous cyclic hardening surpasses the peak stress of the CoCrFeNiMn alloys. On the other hand, the DED CoCrFeNiMn has a higher initial peak stress, but it undergoes little hardening, followed by rapid softening. The HR CoCrFeNiMn shows a secondary cyclic-hardening behavior after softening. The fatigue life and fatigue strength are presented in Fig. 2e and Table S2. These results indicate that CoCrNi alloys have much greater fatigue performance in terms of the cyclic strength and fatigue life, compared to the CoCrFeNiMn alloys. In addition, HR alloys have a better fatigue life than those of the DED alloys. The plastic strain energy density (SED) from a fatigue hysteresis loop per specific cycle (Fig. S3) are used to criteria for fatigue life prediction and SED has a proportional relationship with fatigue damage capacity [2,67]. The evolutions of SED are shown in Fig. 2c. The CoCrNi alloys have a superior SED compared to the CoCrFeNiMn alloys within the same manufacturing process. The SED of the HR alloys shows a remarkable increase, relative to the initial value. Meanwhile, DED alloys reveal a continuous decrease in SED until failure, but they consistently have a higher SED than that of the HR alloys for the same alloy type. Fig. 2f shows the fatigue life for the studied alloys and the reported alloys in the literature at various strain amplitudes. The fatigue life of the CoCrFeNiMn HEA is slightly better, compared to the lightweight alloys but worse than the steels and the CoCrNi MEA. The studied HR and DED CoCrFeNiMn reveal a similar fatigue life to the previously reported CoCrFeMnNi HEA alloys and AlCoCrFeNi entropy alloys. On the other hand, HR and DED CoCrNi exhibit a superior fatigue life compared to the reported alloys in the literature.

3.3. *In-situ neutron-diffraction analysis*

Fig. 3, Fig. 4, Fig. S4, and Fig. S5 show in-situ neutron-diffraction results of monotonic tension and LCF experiments along the longitudinal (LD) and transverse (TD) direction. Both the DED CoCrNi and DED CoCrFeNiMn alloys exhibit anisotropic lattice-strain behavior during tension, following the order of {220}, {111}, {311}, and {200} from soft to hard grain in terms of tendency to yield (Fig. S4a and S4b). The grain-level deformation behavior is similarly reported in polycrystalline face-centered-cubic (FCC) alloys. The diffraction peak intensities of the DED

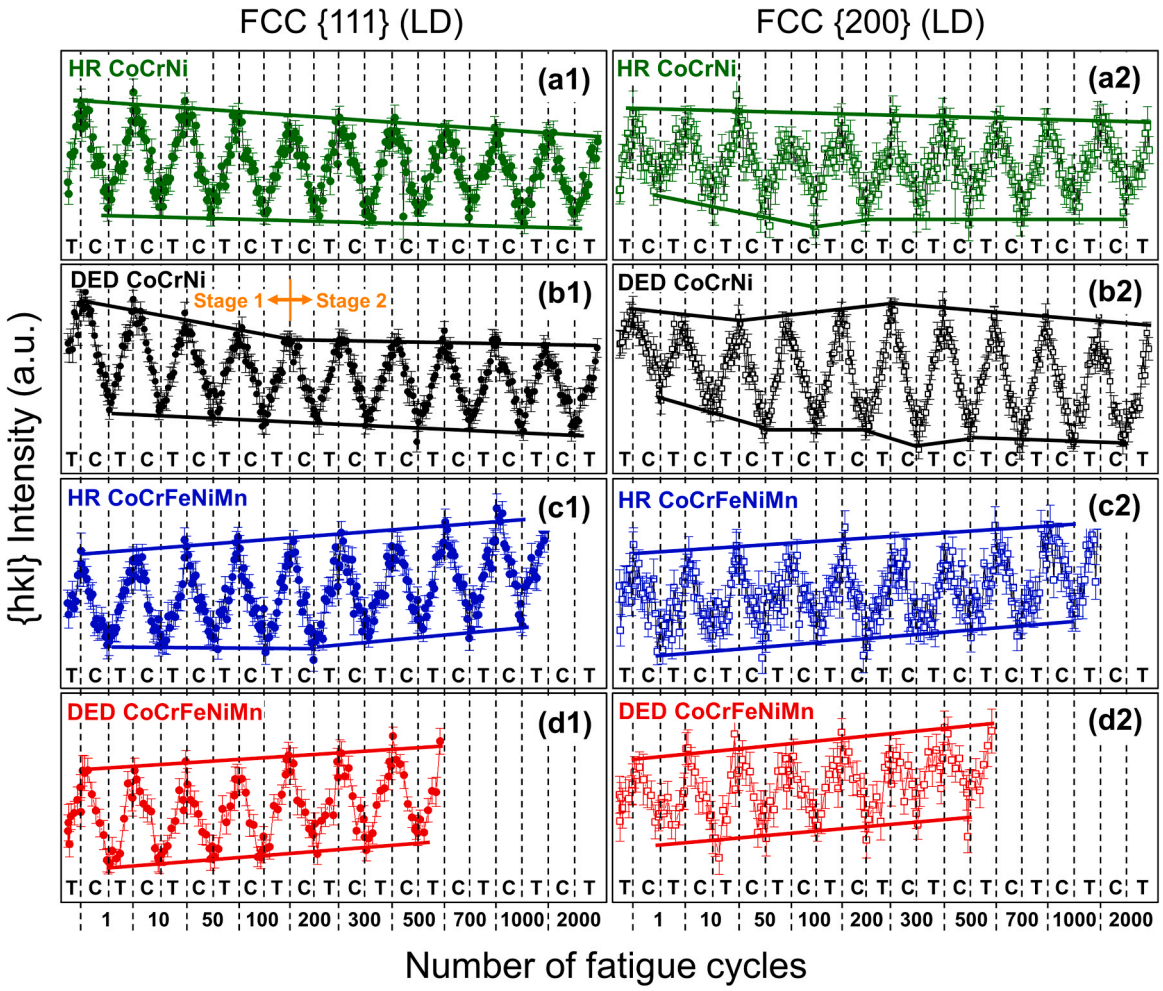

Fig. 3. Neutron-diffraction analyses of low cycle fatigue test: {hkl} intensity evolution as a function of number of fatigue cycles on (a1) FCC {111} and (a2) FCC {200} for the HR CoCrNi, (b1) FCC {111}, and (b2) FCC {200} for the DED CoCrNi, (c1) FCC {111} and (c2) FCC {200} for the HR CoCrFeNiMn, (d1) FCC {111}, and (d2) FCC {200} for the DED CoCrFeNiMn (Note that T is tension, and C is compression).

CoCrNi and DED CoCrFeNiMn alloys remain unchanged in the elastic regime, but a divergence in the diffraction intensity is observed during plastic deformation (Fig. S4c and S4d). The intensities of the {111}, {200}, and {311} grain families increase in the LD but decrease in the TD. Conversely, for the {220} grain, the intensity decreases in the LD but increases in the TD (Fig. S4c and S4d). This phenomenon is observed when the dislocation slip is the primary deformation mechanism in the FCC structure. The LCF-experiment results also reveal an anisotropic lattice-strain behavior in both the CoCrNi and CoCrFeNiMn alloys (Fig. S4e ~ S4h). The soft grain family, {111}, almost exhibits a linear behavior, while the hard grain family, {200}, reveals a larger hysteresis loop during the fatigue cycles. These results indicate that the hard {200} grains absorb more energy from external fatigue stresses compared to the soft {111} grains.

Figs. 3 and 4 show the {hkl} intensity and full width at half maximum (FWHM) response during the LCF experiments for the CoCrNi and CoCrFeNiMn alloys. Deformation mechanisms, such as dislocation slip, mechanical twinning, and strain-induced phase transformation, in the FCC alloy during cyclic deformation can be dynamically characterized using in-situ neutron diffraction [79–82]. The overall trend in the diffraction peak intensities and the FWHMs of {111} and {200} increase for both the HR CoCrFeNiMn and DED CoCrFeNiMn as a function of the fatigue cycles (Fig. 3c, 3d, 4c, and 4d). These trends indicate that dislocation slip-based deformation is predominant in the CoCrFeNiMn alloys. Interestingly, we observe a noticeable decrease in the peak intensity for the {111} grain family in both the HR and DED CoCrNi alloys. The {200} grain family also shows a decreasing and/or saturation trend in the peak intensity (solid lines in Fig. 3a and 3b), although this trend is not as prominent as that observed in the {111} grain family. Moreover, the HR CoCrNi and DED CoCrNi exhibit an abnormal increase in the FWHM at an early stage (Fig. 4a and 4b). The decrease in intensity and the abnormal increase in FWHM result from the evolution of nano-twins rather than the simple dislocations mechanism [20].

One notable observation in the CoCrNi alloys is that the peak intensity of {111} decreases even more in tension than in compression (Fig. 3a1 and 3b1), while for the {200} grains, intensity decreases more in compression than in tension (Fig. 3a2 and 3b2). More interestingly, it is observed that the intensity of the {111} grains of the DED CoCrNi decreases sharply up to 100 cycles in the tension (Stage 1 in Fig. 3b1), followed by a gradual decrease until fracture (Stage 2 in Fig. 3b1). Furthermore, only the DED CoCrNi reveals a strain-induced HCP phase transformation, as shown by the increase of the {10.1} HCP diffraction peak after 500 fatigue cycles (Fig. S5). However, phase transformation does not occur during the tensile experiment (Fig. S4c and S4d). This feature suggests that the tension-compression cyclic deformation promotes new deformation mechanisms in the DED CoCrNi. A detailed discussion of these results is provided in the discussion section.

3.4. Microstructure analysis after fatigue tests

Fig. 5 shows the ECCI and EBSD analyses results of the CoCrNi alloys after fatigue tests (comprehensive results of the EBSD microstructural

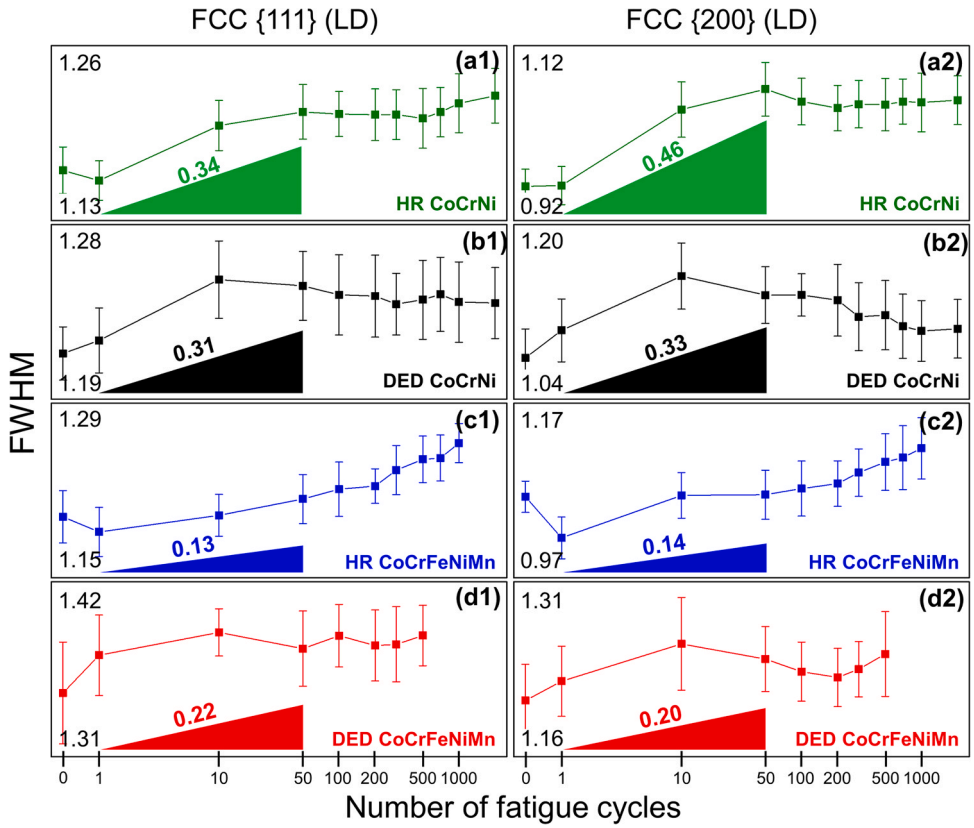

Fig. 4. FWHM as a function of the number of fatigue cycles on (a1) FCC {111} and (a2) FCC {200} for the HR CoCrNi, (b1) FCC {111} and (b2) FCC {200} for the DED CoCrNi, (c1) FCC {111} and (c2) FCC {200} for the HR CoCrFeNiMn, (d1) FCC {111} and (d2) FCC {200} for the DED CoCrFeNiMn.

analyses are presented in Fig. S6). A new deformed microstructure, appearing as white rods, is generated in the HR CoCrNi (Fig. 5a), recognized as mechanical nano-twins (Fig. 5b and 5c). The DED CoCrNi also has a distinct microstructure similar to the HR CoCrNi after fatigue testing (Fig. 5d). It is confirmed that a new HCP phase evolves alongside the mechanical nano-twins. These multiple microstructures observed in the DED CoCrNi are classified into three types: (1) solely nano-twins, (2) solely HCP phases, and (3) a coexistence of nano-twins and HCP phases (Fig. 5e3 and 5f3). The crystallographic relationship of the FCC matrix, FCC twin, and HCP phase satisfies the following Shoji-Nishiyama (S-N) orientation relationship [83]: $\{111\}_{FCC}$ // $\{111\}_{Twin}$ // $\{0001\}_{HCP}$, $<011>_{FCC}$ // $<011>_{Twin}$ // $<2\bar{1}\bar{1}0>_{HCP}$ (Fig. S7). Based on the neutron-diffraction (Fig. S5) and EBSD (Fig. 5e and 5f) analyses results, it is revealed that mechanical nano-twins evolve first from the FCC matrix, and the HCP phases subsequently develop from the nano-twins.

Fig. 6 shows the results of the ECCI analyses at high magnification on fatigue-fractured samples. Dislocations are seldom found in the HR CoCrNi and HR CoCrFeNiMn in the initial state (Fig. 6a and 6i). However, the DED CoCrNi and DED CoCrFeNiMn exhibit significant dislocations even in the initial state (Fig. 6e and 6m). Especially, the DED CoCrNi has stacking faults in the initial state (Fig. 6e). A significant number of nano-twins develop in the HR CoCrNi after cyclic deformation (Fig. 6b), as confirmed by the EBSD analysis (Fig. 5). In addition, the HR CoCrNi has considerable stacking faults as well as nano-twins, and dislocations are severely tangled with both the stacking faults and nano-twins (Fig. 6c and 6d). Furthermore, low energy dislocation structures, such as dislocation wall and cell structures, are slightly formed in the HR CoCrNi (Fig. 6c and 6d). The DED CoCrNi has a large number of nano-twins and HCP phases compared to the HR CoCrNi (Fig. 6f), but the presence of stacking faults in the DED CoCrNi is lower compared to the HR CoCrNi (Fig. 6c, 6d, 6g, and 6h). Dislocations in the DED CoCrNi are tangled with stacking faults, nano-twins, and HCP phases. However, unlike the HR CoCrNi, the DED CoCrNi has no dislocation wall or cell structures (Fig. 6g and 6h). The HR CoCrFeNiMn has many dislocation cell structures (Fig. 6k) and some mechanical nano-twins (Fig. 6j and 6l). On the other hand, there are no nano-twins in the DED CoCrFeNiMn, while numerous dislocation cell structures are observed (Fig. 6o and 6p).

3.5. *Convolutional multiple whole profiles (CMWP) analysis*

The CMWP analyses results for the four types of alloys are shown in Fig. 7. Intrinsic stacking-fault (ISF) probability of the HR CoCrNi and HR CoCrFeNiMn show similar values. At the same time, the DED CoCrNi has two times higher ISF probability than that of the HR alloys. The ISF probability of the DED CoCrFeNiMn represents the intermediate value between the DED CoCrNi and HR alloys. Regarding the extrinsic stacking-fault (ESF) probability, the DED CoCrNi still has the highest value, and the HR CoCrFeNiMn has the lowest value. However, the order in the ESF probability differs from the case of the ISF probability. The CoCrNi alloys have a higher twin fault (TF) probability than that of the CoCrFeNiMn alloys. The highest TF probability is seen in the DED CoCrNi, followed by the HR CoCrNi, HR CoCrFeNiMn, and DED CoCrFeNiMn. The results of the TF probability reveal a similar tendency to the microstructure analysis by ECCI (Fig. 6). The ESF and TF probabilities of the studied alloys, except for the DED CoCrNi, exhibit an increased tendency at the early cycles; within 10 cycles for the HR CoCrNi and DED CoCrFeNiMn, and within 50 cycles for the HR CoCrFeNiMn. This is followed by a subsequent decrease up to 100 cycles for the DED CoCrFeNiMn, 200 cycles for the HR CoCrNi, and 300 cycles for the HR CoCrFeNiMn. This trend is consistent with the macroscopic hardening and softening behavior shown in the cyclic-stress responses (Fig. 2b). In the later stage of the fatigue cycles, each probability value starts to increase again due to the formation of a local stress field. The DED CoCrNi maintains the highest probabilities for ISF, ESF, and TF

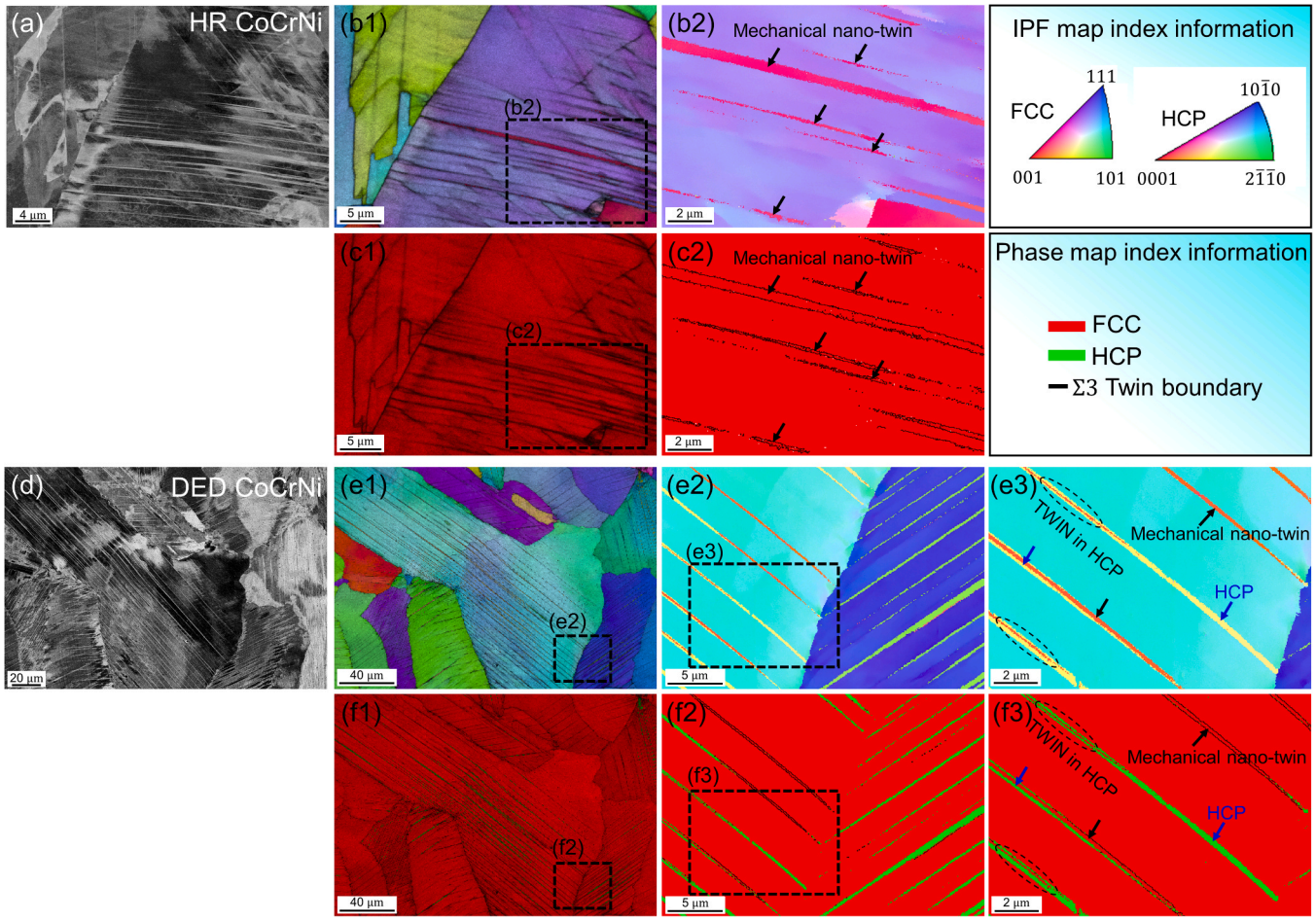

Fig. 5. Microstructure-analysis results after fatigue failure: (a) ECCI image, (b) EBSD-IPF map, and (c) EBSD-phase map for HR CoCrNi; (d) ECCI image, (e) EBSD-IPF map, and (f) EBSD-phase map for DED CoCrNi. Note that all of microstructure-analysis are conducted on cross-section perpendicular to the loading direction of cylindrical sample.

during cyclic deformation. However, the ESF and TF probabilities of the DED CoCrNi continuously decrease after 300 cycles.

3.6. Fractography analysis

Fig. 8 shows the fractography for the four types of alloys. We observe that crack initiates at the sample surface and propagates inward. Interestingly, based on previous microstructural analyses, we expect the cracks to initiate from defects due to the large amounts of micro- and nano-porosity found in DED alloys (Fig. 1j and 1l). However, contrary to our concerns, we observe that the crack initiation sites in all types of samples originate not from pores or similar defects, but directly from the microstructural matrix (Fig. 8a2-d2). According to well-known research, defects present in alloys with brittle characteristics play a crucial role in leading to crack initiation [50,58]. In contrast, alloys with excellent ductility are known to have a lower contribution of defects to crack initiation [58]. For this reason, it is confirmed that the micro- and nano-porosity developed in the DED CoCrNi and DED CoCrFeNiMn with superior ductility do not have a significant impact on crack initiation. Nevertheless, it reveals that such micro- and nano-porosity degrade the fatigue crack propagation properties [56] (This will be discussed in session 4.4). The crack propagation path in the CoCrFeNiMn alloys is almost straight (Fig. 8c3 and 8d3). In contrast, the crack-propagation path in the CoCrNi alloys exhibits a zig-zag shape, which can be attributed to the presence of nano-twins and HCP phases (Fig. 8a3 and 8b3) [84,85]. Fatigue striations are observed in the HR CoCrNi and DED CoCrNi (Fig. 8a4 and 8b4). The length of the fatigue striation (measured by adding up five striations) in the DED CoCrNi is greater than that of the HR CoCrNi. This observation implies that the crack-propagation rate of the DED CoCrNi is faster than that of the HR CoCrNi. Fatigue striation is also found in the HR CoCrFeNiMn, and their length is similar to that of the HR CoCrNi (Fig. 8c4). However, fatigue striation is hardly found in the DED CoCrFeNiMn (Fig. 8d4). The higher crack-growth rate in the DED CoCrFeNiMn is attributed to the activation of a single deformation mode governed by dislocation slip, which results in a quasi-cleavage fracture (Fig. 8d4).

4. Discussion

4.1. Strain localization on the nano-twins

The critical twinning stress of the CoCrNi and CoCrFeNiMn are known to be 790 ± 100 and 720 ± 3 MPa, respectively [86]. However, all of the studied alloys, except for the DED CoCrFeNiMn, exhibit mechanical nano-twins during the cyclic deformation (Fig. 6), even though the applied maximum stress is lower than the critical twinning stress (Fig. 2b). The DED CoCrFeNiMn exhibits a dislocation cell structure without any mechanical twinning after fatigue (Fig. 6o and 6p) because the medium SFE of the CoCrFeNiMn alloys at room temperature is sufficiently high to induce the dislocation slip deformation [26,87]. As a result, it is difficult to develop mechanical twinning below the critical twinning stress level. Similarly, the HR CoCrFeNiMn also shows a dislocation cell structure after fatigue due to the medium SFE (Fig. 6k). However, mechanical nano-twins are often observed in the HR

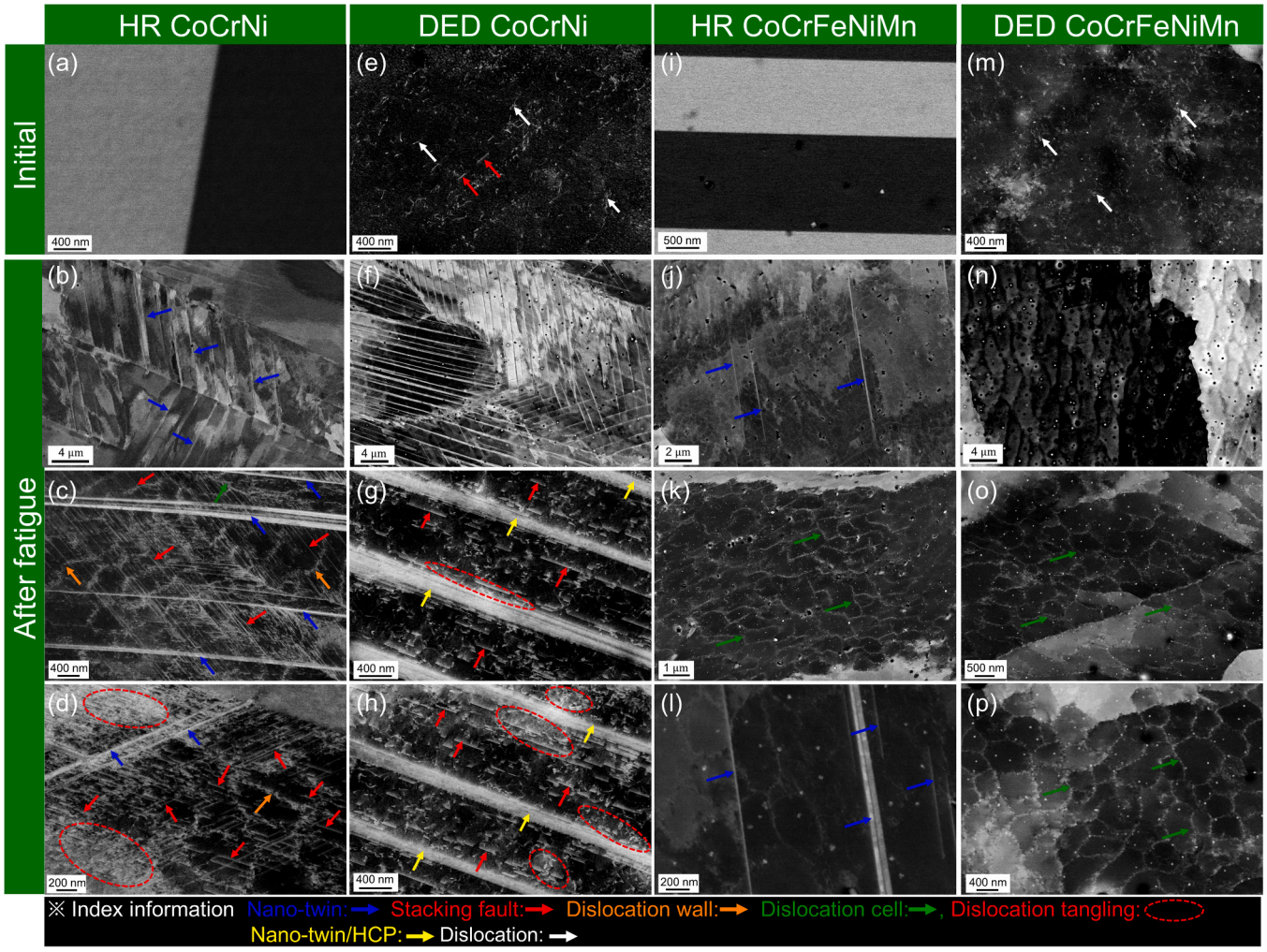

Fig. 6. ECCI microstructure-analysis results: HR CoCrNi (a) in the initial state and (b-d) after fatigue testing, DED CoCrNi (e) in the initial state and (f-h) after fatigue testing, HR CoCrFeNiMn (i) in the initial state and (j-l) after fatigue testing, and DED CoCrFeNiMn (m) in the initial state and (n-p) after fatigue testing. Note that all of microstructure-analysis are conducted on cross-section perpendicular to the loading direction of cylindrical sample.

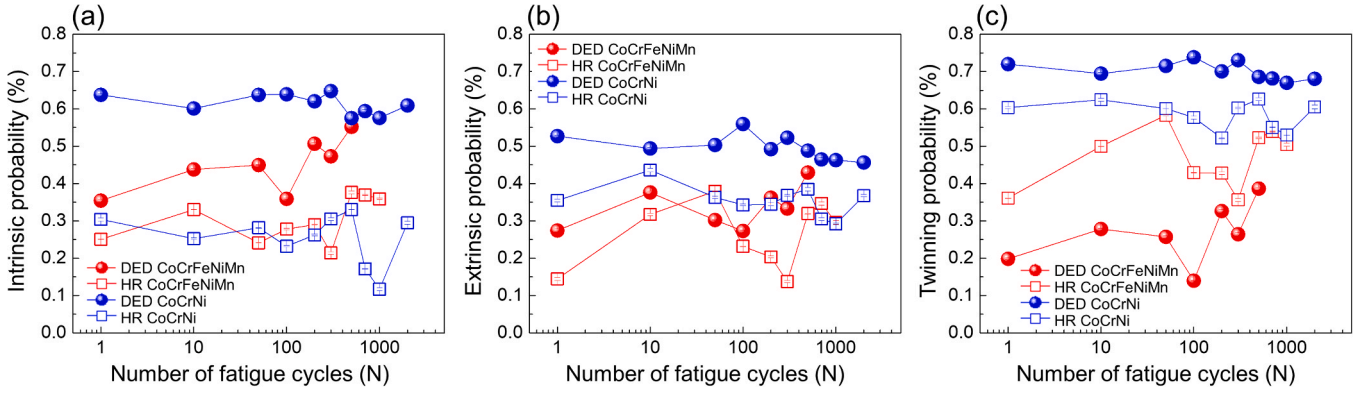

Fig. 7. CMWP-analysis results: (a) intrinsic stacking-fault probability, (b) extrinsic stacking-fault probability, and (c) twin-fault probability.

CoCrFeNiMn (Fig. 6j and 6l), despite having a medium SFE and undergoing lower peak stresses than the DED CoCrFeNiMn (Fig. 2b). One possibility is that as the crack propagates, the stress concentration at the crack tip creates a significant plastic zone, which can result in stresses higher than the critical twinning stress, leading to the formation of mechanical twinning. Moreover, we conduct TEM analysis to perform an in-depth investigation of the cause for these results. Fig. 9 shows the TEM images of the HR CoCrFeNiMn and HR CoCrNi after fatigue deformation. We find that a clear dislocation-cell structure is formed (Fig. 9a), which is the same result as the ECCI image (Fig. 6k). Especially, mechanical nano-twins tend to develop in the vicinity of the high strain area, where the dislocation tangling and dislocation cell boundary are present (Fig. 9b). This phenomenon can be elucidated by the following reasons. As dislocations move forward and backward during

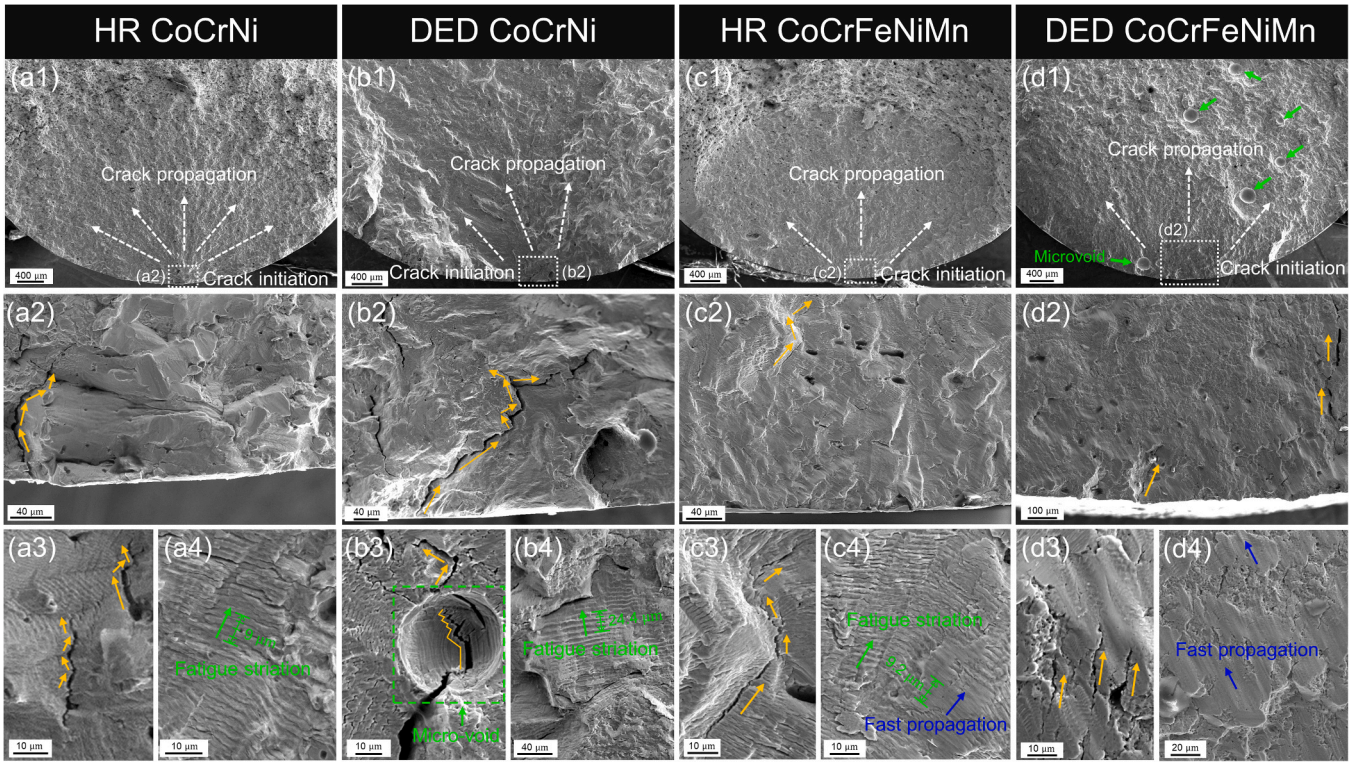

Fig. 8. Fractography for (a1-a4) HR CoCrNi, (b1-b4) DED CoCrNi, (c1-c4) HR CoCrFeNiMn, and (d1-d4) DED CoCrFeNiMn; (a1-d1) show the configuration of crack initiation site and crack propagation, (a2-d2) are high magnification image of crack initiation site, (a3-d3) show the image of crack propagation, and (a4-d4) show image of fatigue striation.

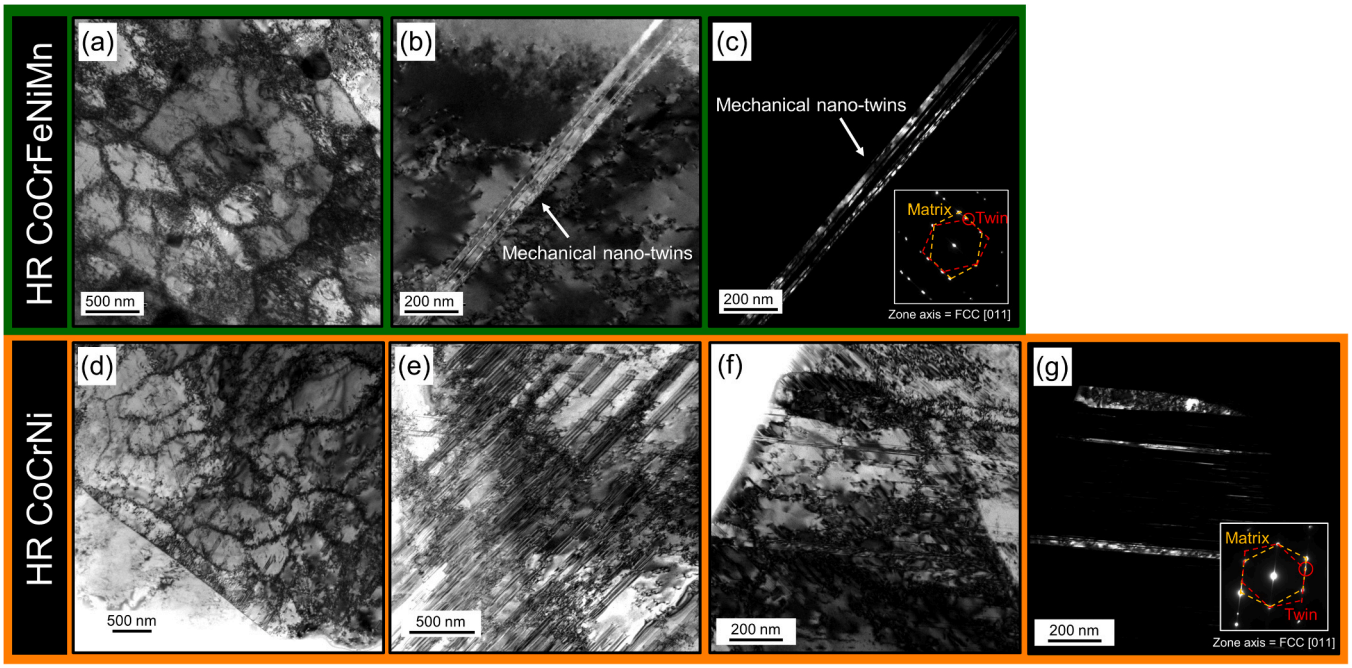

Fig. 9. TEM image of the HR CoCrFeNiMn after fatigue testing: (a) dislocation-cell structure by the bright-field image, (b) nano-twins by the bright-field image, and (c) nano-twins by the dark-field image with the SAED pattern; TEM image of the HR CoCrNi after fatigue testing: (d) dislocation-cell structure by the bright-field image, (e) stacking faults by the bright-field image, (f) nano-twins by the bright-field image, and (g) nano-twins by the dark-field image with a SAED pattern. Note that all of microstructure-analysis are conducted on cross-section perpendicular to the loading direction of cylindrical sample.

cyclic deformation, they become entangled, forming a low energy dislocation structure for energy stabilization, such as dislocation cell structures. The dislocation sub-structure leads to the formation of a high strain field and results in localized stress concentrations, which provoke the development of mechanical nano-twins. However, in the case of the DED CoCrFeNiMn, the development of nano-twins is challenging

because the TF probability of the DED CoCrFeNiMn is the lowest, compared to the other alloys (Fig. 7c). Distinct microstructures of a dislocation cell structure (Fig. 9d), stacking faults (Fig. 9e), and nano-twins (Fig. 9f and 9g) are observed in the HR CoCrNi. We confirm that numerous stacking faults and nano-twins develop near the high strain field. Furthermore, the HR CoCrNi alloys have a large amount of stacking faults and nano-twins compared to the HR CoCrFeNiMn alloys due to the low SFE (22 ± 4 mJ/m^2 for the CoCrNi and 30 ± 5 mJ/m^2 for the CoCrFeNiMn [26,86]).

4.2. Anisotropic-microstructure evolution

Based on the microstructure results of the HR and DED CoCrNi alloys (Figs. 5, 6, and 9), we confirm that the decrease in the peak intensities of {111} and {200} (Fig. 3a and 3b) and the abnormal increase in the FWHMs (Fig. 4a and 4b) are due to the formation of numerous nano-twins. The {111} peak intensity of HR and DED CoCrNi decrease throughout all the fatigue cycles (Fig. 3a1 and 3b1). Especially, the reduction in the {111} peak intensity of the HR and DED CoCrNi is more pronounced at + 1 % (tension direction), compared to −1 % (compression direction), but the reduction in the {200} peak intensity is more prominent at − 1 %. This feature proves that the microstructure evolution under tension and compression exhibits anisotropic characteristics. To comprehend the mechanism of the anisotropic twin formation, we focus on the correlation between partial dislocations, which are the origin of the twins, and the resolved shear stresses depending on the crystallographic loading direction. The relationship between the resolved shear stresses on the leading and trailing partial dislocations is crucial in developing the stacking faults, twinning, and HCP-phase formation. It is well known that a stacking fault develops easily when the shear stress of the leading partial is higher than that of the trailing partial [82,88]. Fig. 10 shows the resolved shear stress of the leading and trailing partial dislocations on {111} and {200} calculated by the Schmid factor for the Shockley partial dislocations (leading and trailing partials). The Schmid factors for the partial dislocations and their corresponding movable directions during fatigue testing are calculated from two crystallographic orientations: 111_{FCC} and 001_{FCC}. Detailed information regarding these calculations is presented in Table S3, and Figs. S8 and S9. In the 111_{FCC} crystallographic orientation, the leading partial dislocation exhibits a higher Schmid factor than the trailing partial dislocation in tension (Table S3). This difference in the Schmid factors leads to a higher resolved shear stress for the leading partial compared to the trailing partial at the {111} grains during tension (Fig. 10). However, the situation is inverted in compression. In this case, the Schmid factor of the trailing partial is higher, compared to the leading partial for the 111_{FCC} (Table S3). Therefore, the trailing partial experiences a higher shear stress than the leading partial for the {111} grain in compression (Fig. 10). In contrast to the 111_{FCC} orientation, the 001_{FCC} orientation exhibits the opposite behavior. The trailing partial has a larger Schmid factor than the leading partial in tension, while the Schmid factor of the leading partial is higher than that of the trailing partial in compression (Table S3). This trend indicates that the resolved shear stress of the leading partial on the {200} grain is higher in compression. In comparison, the resolved shear stress of the trailing

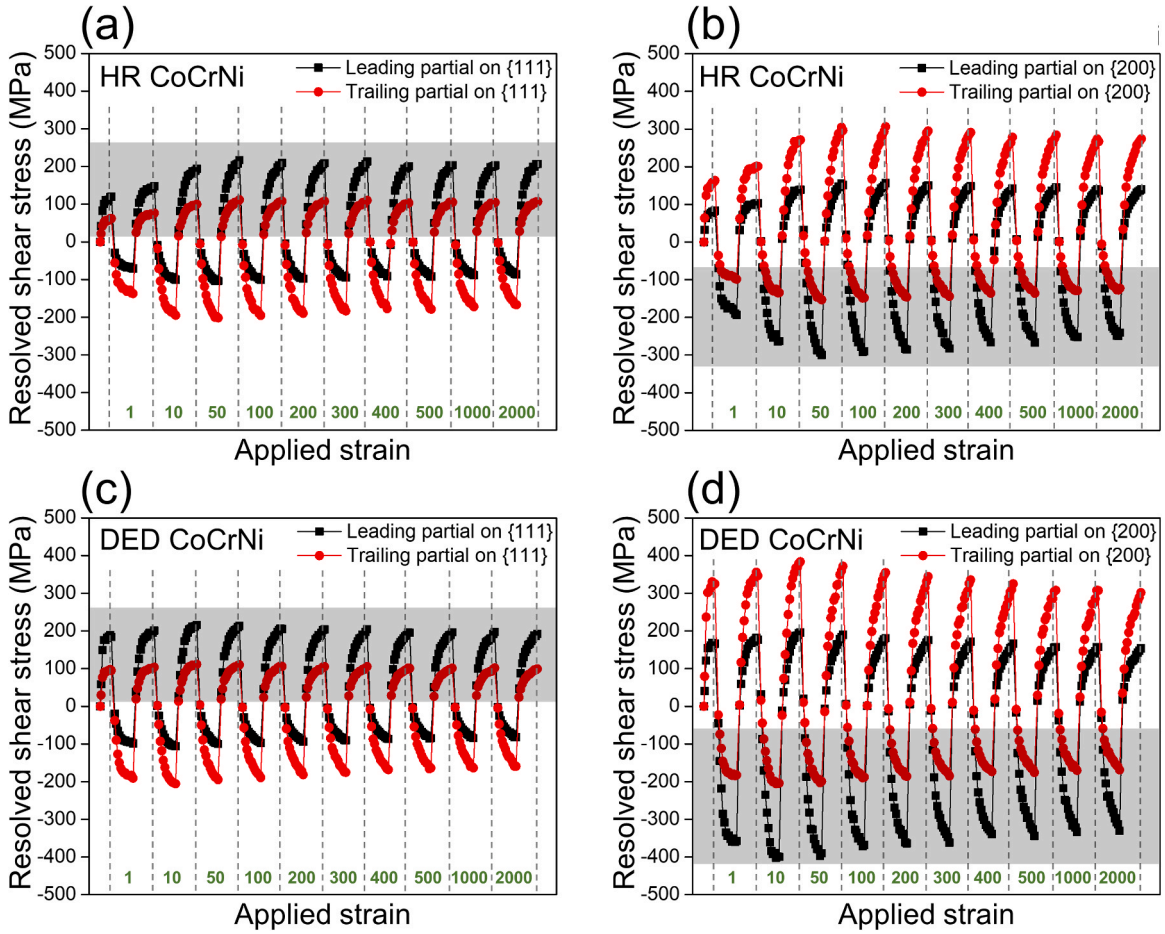

Fig. 10. The resolved shear stress of the leading and trailing partial dislocations on {111} and {200} calculated by the Schmid factor for the Shockley partial dislocations: (a) {111} of HR CoCrNi, (b) {200} of HR CoCrNi, (c) {111} of DED CoCrNi, and (d) {200} of DED CoCrNi (Note that the numbers 1, 10, 50 ⋯ 2000 indicate fatigue cycles, and the black shadow is a region where the leading partial has higher resolved shear stress than the trailing partial).

partial is higher in tension (Fig. 10). Based on these findings, we conclude that nano-twins are developed prominently in the {111} grain under tension, while they are more likely to be formed in the {200} grain under compression. Consequently, this phenomenon leads to a notable decrease in the diffraction intensity of the {111} grains at strains of + 1 % (in tension) and the {200} at strains of − 1 % (in compression) for HR and DED CoCrNi alloys (Fig. 3a and 3b). Another interesting phenomenon involving the anisotropic-intensity behavior is observed in the DED CoCrNi. Specifically, the {111} peak intensity of the DED CoCrNi at + 1 % experiences a notable reduction up to 100 cycles (Stage 1 in Fig. 3b1), followed by a gradual decrease (Stage 2 in Fig. 3b1). These results indicate that significant quantities of mechanical nano-twins are formed up to 100 cycles in the DED CoCrNi, particularly under tension. To understand this phenomenon, we compare the resolved shear stresses on the {111} and {200} grain families for the HR and DED CoCrNi in the earlier cycles up to 100 cycles. Notably, the resolved shear stresses on the {111} and {200} grains for the DED CoCrNi are higher than those of the HR CoCrNi at the early stage, as seen in Fig. 10. These results are explained by the fact that DED CoCrNi exhibits high residual stress (Fig. 1f), high initial dislocation density (Fig. 6e), and different microstructural textures at the initial state (Fig. S10). The HR CoCrNi has the normal rolling texture. On the other hand, a different texture is developed in the DED CoCrNi due to the directional grain growth depending on the scanning path and building direction. Specifically, the {111}, {200}, and {220} orientations exhibit growth at intervals of 90 degrees, and the {111} and {220} orientations have a relationship with the {200} orientation at an angle of ~ 45 degrees (Fig. S10). This unique initial microstructure of the DED CoCrNi leads to the high resolved shear stress on each partial dislocation, even in the early stage. Therefore, a substantial number of nano-twins could develop in the DED CoCrNi at the early stage, which provides a considerable decrease in the {111} diffraction intensity of the DED CoCrNi in tension until Stage 1 (Fig. 3b1).

4.3. Effective stacking-fault energy

The HCP-phase transformation does not occur in the DED CoCrNi during tensile tests at room temperature (Fig. S4c). However, it is confirmed that the HCP phase transformation occurred in the DED CoCrNi during LCF even at room temperature (Fig. S5) where the maximum stress is only 652 MPa (Table S2). In contrast, the HR CoCrNi does not undergo any phase transformation during fatigue despite having the same chemical composition as the DED CoCrNi. Interestingly, the dislocation wall and cell structures are only observed in the HR CoCrNi. In contrast, no low energy dislocation structure is observed in the DED CoCrNi (Fig. 6). This trend implies that nearly all perfect dislocations in the DED CoCrNi dissociate into partial dislocations to form stacking faults, nano-twins, and HCP phases instead of building up the dislocation wall and/or cell structures. Understanding SFE is essential for predicting deformation behavior and improving mechanical properties of FCC alloys. Meanwhile, calculating the SFE of metastable-entropy alloys that consist of various elements is highly challenging compared to traditional metals [89,90]. Moreover, the SFE of these alloys possesses a variable local property due to the chemical complexity whose phenomena lead to unique plasticity mechanisms and controllable mechanical properties [27,91]. Especially, the microstructural characteristics such as the chemical distribution of atoms, elemental segregation of solute atoms, defects, lattice distortion, and strain fields near stacking faults reduce the SFE [92–94]. Based on the microstructure analysis of the DED CoCrNi, it is found that both numerous dislocations (Fig. 6e) and high residual stress (strain fields) are generated at the initial state (Fig. 1e and 1f) when compared to the HR CoCrNi. These factors decrease the energy barrier of the stacking fault formation, leading to a reduction in the effective SFE in the localized region. Moreover, when considering the macroscopic fatigue behavior, the DED CoCrNi exhibits a substantial capacity to accumulate the strain energy per fatigue cycle (Fig. 2c). Therefore, a low effective SFE due to the presence of numerous dislocations and stacking faults at the initial state (Fig. 6e) combined with high strain energy helps overcome the critical stress required for the formation of both nano-twins and HCP phases. The mechanical nano-twins serve as nucleation sites for the subsequent formation of the HCP structure. Consequently, the synergy of these factors ultimately leads to the evolution of HCP phases in the DED CoCrNi after 500 cycles. Moreover, the DED CoCrNi has a higher probability of ISF and ESF compared to the HR CoCrNi (Fig. 7). The HCP phase is typically developed from the ISF that occurs every two layers (Fig. S11). The ISF probability of the HR CoCrNi is lower than the ESF. However, in the case of the DED CoCrNi, the ISF probability is higher than the ESF probability, and the ESF probability of the DED CoCrNi continuously decreases after 300 cycles (Fig. 7), which accounts for the formation of the HCP phases in the DED CoCrNi after 500 cycles.

4.4. Fatigue fracture and damage mechanism

The DED process exhibits a lower fatigue life compared to the HR process in the same type of alloys. Specifically, the DED CoCrNi exhibits an 11 % reduction in fatigue life compared to the HR CoCrNi. The DED CoCrFeNiMn has a 26 % worse fatigue life than the HR CoCrFeNiMn (Fig. 2b and 2e). One major reason for the inferior fatigue resistance of the DED alloys is the development of defects, including micro- and nano-porosity, which accelerates crack propagation. If the porosity can be effectively controlled while maintaining the intrinsic microstructures of the DED alloys, it is expected that their fatigue life can be much improved [57]. The difference in fatigue deformation mechanisms between DED alloys is that nano-twins and HCP phase are evolved in DED CoCrNi (Fig. 11a), while dislocation cell structure is developed in the DED CoCrFeNiMn (Fig. 11d). The growth of nano-twins and HCP phases in DED CoCrNi occurs in a straight line without being impeded by the solidification cell structure (Fig. 11a). In particular, nano-porosity are located between the finely developed nano-twins and HCP phases (blue arrow in Fig. 11a), and in some cases, they are observed to be trapped within nano-twins and HCP phases (blue circle in Fig. 11a). However, the dislocation cell structure in DED CoCrFeNiMn is too small to contain nano-porosity, and rather the nano-porosity hinders the formation of the dislocation cell structure (Fig. 11d). In addition, micro- and nano-porosity do not initiate main crack, but promote crack propagation (Fig. 11b and 11e). The microstructure of the DED CoCrFeNiMn, consisting of large columnar grains, fine grains formed near the melt pool boundary, solidification cell structure, and dislocation cell structure (Figs. 1d, 6n, 6o, and 6p), does not effectively help to enhance fatigue resistance and allows for the crack propagation in a nearly straight manner along the porosity. However, the DED CoCrNi shows interesting outcomes due to the differences in deformed microstructure, although the crack propagates along the porosity similar to the DED CoCrFeNiMn (white arrow in Fig. 11b). Mechanical nano-twins and HCP phase that generate in the DED CoCrNi play a crucial role in the crack propagation behavior. The boundaries of deformed microstructure (nano-twins and HCP phase) act as a barrier to hinder the crack propagation by generating crack deflection and branching (Fig. 11b). Especially, when the boundaries of twins and HCP phase are nearly perpendicular to the crack propagation direction, the delaying action of crack propagation is more significant (dashed line in Fig. 11c). The consecutive crack blunting and deflection gives rise to zig-zag fracture with the formation of sub-cracks. Consequently, the distinctive microstructural features, such as nano-twins and HCP phase, formed in the DED CoCrNi promote crack branching/bridging (Fig. 11b,c), which mitigates stress concentrations at the crack tip. This reduces the driving force of the crack propagation, leading to lower crack-growth rates in the DED CoCrNi alloys [84,85,95]. Evidently, this mechanism is clearly observed in Fig. 8b3 (green box), where the crack propagates into the micro-pores, but the nano-twins and HCP phases change the crack propagation path, leading to a hindering effect that prevent further crack propagation. Based on

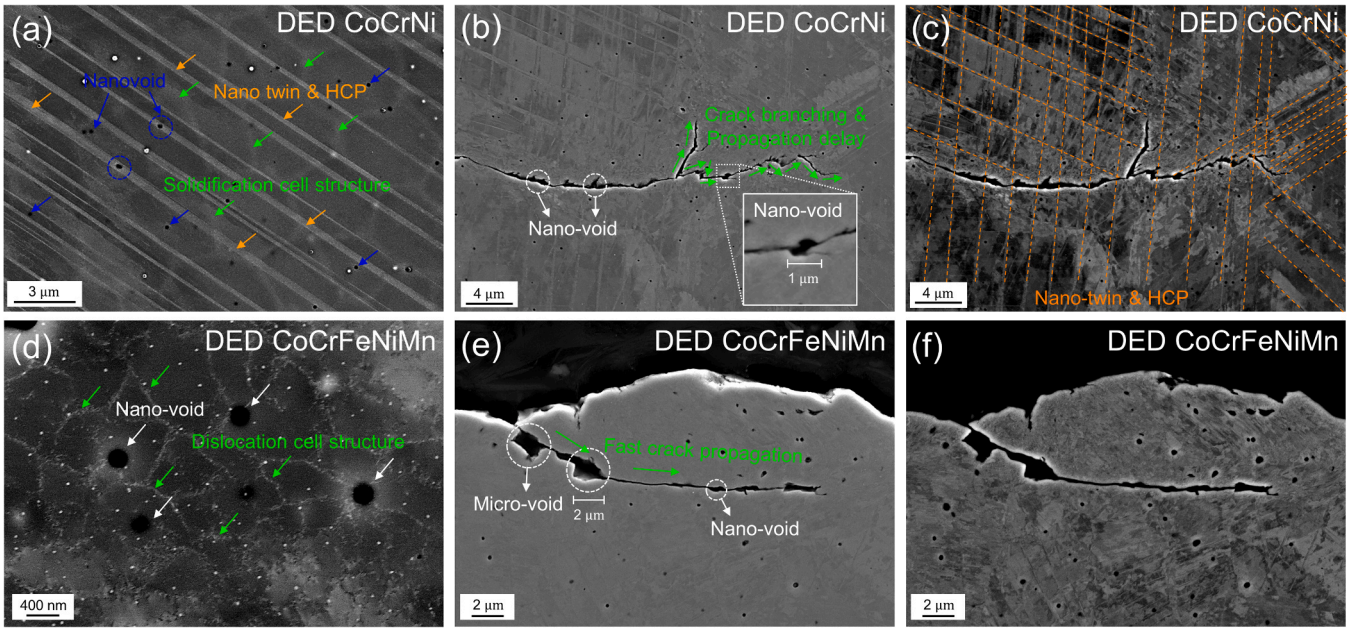

Fig. 11. Microstructure analysis after fatigue deformation; SEM image of the cross section for (a, b) DED CoCrNi and (e) DED CoCrFeNiMn, and ECCI image of the cross sections for (c) DED CoCrNi and (d, f) DED CoCrFeNiMn (Note that we added auxiliary lines in (c) corresponding to the Twin and HCP phase for comparison).

these results, multiple deformation mechanisms of the DED CoCrNi results in better fatigue properties compared to the DED CoCrFeNiMn that relies on a single dislocation slip mode. In particular, the presence of nano-twins and HCP phases has more beneficial effect on fatigue resistance than existence of solidification cell structure and dislocation cell structure. The limited dislocation hardening potential in DED alloys due to the high initial dislocation density and high residual stress is another reason for the degradation of the fatigue resistance. A high initial dislocation density and residual stress of DED alloys result in a significant increase in the yield strength, thereby leading to excellent cyclic strength and SED in the early fatigue stage. However, as the amount of accumulated deformation increases, softening of the strength occurs in the early stage (Fig. 2b), and the SED decreases steeply (Fig. 2c) because the critical stored energy from dislocation hardening is quickly consumed within a few cycles. Therefore, if it is possible to control the consumption of the dislocation hardening potential sustainably by changing the microstructural characteristics, the DED process is expected to exhibit superior fatigue resistance. Nevertheless, it should be emphasized that the DED CoCrNi has excellent fatigue performance compared to conventional AM alloys (Fig. 2f). This is due to the fact that DED CoCrNi experiences a further reduction in effective SFE by a combination of high dislocation density and high residual stress. This makes it easier to overcome the critical stress for the evolution of nano-twin and HCP phase, thereby promoting a fine and dense structure, which helps prevent the degradation of fatigue endurance. Therefore, the high dislocation density and high residual stress of DED CoCrNi have pros and cons on the fatigue properties. In contrast, DED CoCrFeNiMn, which has a medium SFE, is much less synergistic effect on the fatigue properties.

4.5. Potential methods for improving fatigue properties based on microstructure tuning

We suggest suitable methods to enhance AM fatigue resistance without any post-processing and post heat-treatment. CoCrNi alloys have a superior fatigue life, compared to the CoCrFeNiMn alloys (Fig. 2b and 2e). The HR CoCrNi has a 287 % higher fatigue life, compared to the HR CoCrFeNiMn, and the DED CoCrNi also has a 345 % higher fatigue life than that of the DED CoCrFeNiMn. The excellent fatigue endurance of the HR and DED CoCrNi is attributed to microstructural tuning by controlling the SFE. The low intrinsic SFE of the CoCrNi alloys combined with strain localization makes it more prone to evolving stacking faults and nano-twins, compared to CoCrFeNiMn alloys with higher SFE. The distinct microstructure in the HR and DED CoCrNi highly keeps activating strain hardening and postponing the transition stage from hardening to softening during cyclic deformation (Fig. 2b), thereby delaying crack initiation. Meanwhile, the multiple deformation activities of the CoCrNi alloys promote crack blocking and crack branching/bridging (Fig. 11b and 11c), which reduce the driving force of the crack propagation, thus slowing the crack-growth rate and improving fatigue life. Consequently, the presence of these multiple deformed microstructures has positive effects on improving fatigue resistance. Furthermore, the reduced effective SFE of the DED CoCrNi helps overcome the critical stress required for the formation of multiple deformed microstructures with fine structures that includes a lot of stacking faults and nano-twins as well as HCP phases. This effect helps to further enhance the fatigue properties. The overall understanding of cyclic deformation mechanisms, fracture mechanisms, and micro-crack propagation behavior is summarized in Table 1 and Fig. 12.

5. Conclusions

Low cycle fatigue properties are characterized by in-situ neutron diffraction coupled with multiscale microstructure analysis. We systematically investigate a microstructural design strategy focusing on enhancement in fatigue resistance for high and medium entropy alloys fabricated by direct-energy-deposition and hot-rolling processes. The current work provides an effective method for designing advanced alloys with high fatigue resistance through microstructural tuning that controls the effective stacking fault energy combined with high strain energy density. The major findings of the scientific issue are provided below.

(1) CoCrNi medium-entropy alloys exhibit much more superior fatigue life than CoCrFeNiMn high entropy alloys. Specifically, the HR CoCrNi reveals 287 % higher fatigue life than the HR CoCrFeNiMn, and the DED CoCrNi exhibits 345 % higher fatigue life than that of DED CoCrFeNiMn. The DED process leads to inferior

Table 1
Summary of the differences in microstructural characteristics and fatigue damage mechanisms for high- and medium-entropy alloys depending on the manufacturing process (Note that ● means improvement, ▲ means no significant impact, and x means degradation).

Process type	Alloy type	Initial microstructure	Fatigue properties	Deformed microstructure	Fatigue properties
Hot rolling	CoCrFeNiMn	Equiaxed grain	▲	Dislocation cell structure	x
		Annealing twin	▲	Nano-twin (Small quantity)	▲
	CoCrNi	Equiaxed grain	▲	Nano-twin (Large quantity)	●
		Annealing twin	▲		
Direct energy deposition	CoCrFeNiMn	Large grain	x	Dislocation cell structure	x
		High dislocation density	x		
		High residual stress	x		
		Solidification cell structure	▲		
		Micro- and nano-porosity	x		
	CoCrNi	Large grain	x	Stacking fault (Large quantity)	●
		High dislocation density	▲		
		High residual stress	▲		
		Solidification cell structure	▲	Nano-twin & HCP (Fine and dense structure)	●
		Micro- and nano- porosity	x		

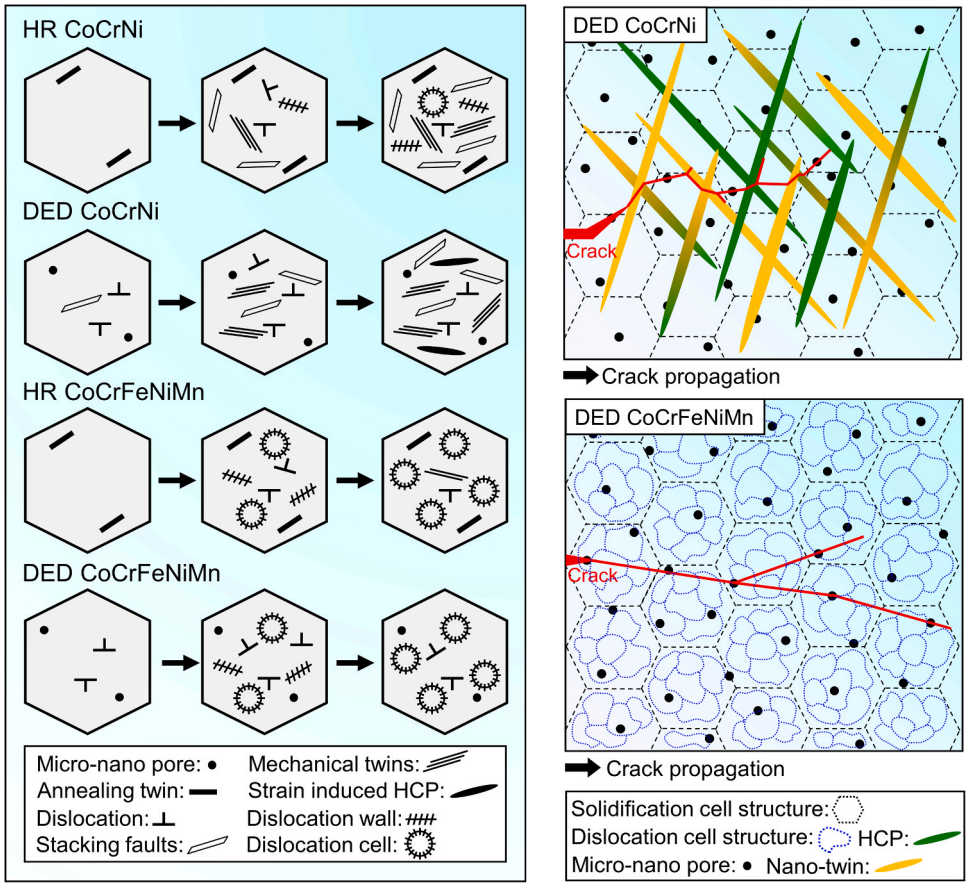

Fig. 12. Schematics of the cyclic deformation mechanism and micro-crack propagation behavior for the CoCrNi and CoCrFeNiMn alloys manufactured by hot rolling and direct energy deposition.

fatigue life compared to the HR process. Specifically, the DED CoCrNi exhibits an 11 % reduction in fatigue life compared to the HR CoCrNi. The DED CoCrFeNiMn has a 26 % worse fatigue life than that the HR CoCrFeNiMn.

(2) Anisotropic microstructure evolution under tension and compression is driven by the relationship between resolved shear stresses on leading and trailing partial dislocations, which is crucial for developing stacking faults and twinning. These findings indicate that nano-twins develop prominently in the {111}

grain under tension and the {200} grain under compression. This effect is pronounced in the DED CoCrNi, where mechanical nano-twins significantly develop up to 100 cycles under tension. It is influenced by high resolved shear stresses of partial dislocation, residual stress, initial dislocation density, and unique micro-structural texture of DED process.

(3) The concurrent evolution of multiple deformed microstructures in CoCrNi alloys, including stacking faults, nano-twins, and hexagonal-close-packed (HCP) structures, effectively hinders the crack propagation and promotes crack branching/bridging during cyclic deformation. Notably, the intrinsic characteristic of low effective stacking fault energy and high capacity of strain energy density for the DED CoCrNi provide the formation of fine-structured nano-twins and HCP phase. This ultimately enhances the fatigue lifetime of the DED CoCrNi compared to other additive manufacturing alloys, despite the presence of numerous micro- and nano-porosity.

(4) Fatigue resistance in the DED process diminishes primarily due to two factors. Firstly, the formation of defects such as micro- and nano-porosity during the DED process promotes crack propagation. Secondly, the inherent high dislocation density in DED alloys limits their dislocation hardening potential, leading to the rapid depletion of critical stored energy within a few cycles. Enhancements in fatigue resistance could be achieved by producing defect-free structures and sustainably managing dislocation energy through microstructural modifications.

CRediT authorship contribution statement

Jayant Jain: Validation, Writing – review & editing. **Peter K. Liaw:** Writing – review & editing, Validation. **Jun Hyun Han:** Writing – review & editing, Validation. **E-Wen Huang:** Writing – review & editing, Validation, Supervision, Formal analysis. **Eunjoo Shin:** Writing – review & editing, Resources. **Wanchuck Woo:** Writing – review & editing, Resources. **Hobyung Chae:** Writing – review & editing, Resources. **Young-Sang Na:** Writing – review & editing, Resources. **Dunji Yu:** Writing – review & editing, Validation, Resources. **Ke An:** Writing – review & editing, Validation, Resources. **Yan Chen:** Writing – review & editing, Validation, Resources. **In-Hwan Oh:** Writing – review & editing, Resources. **Soo Yeol Lee:** Writing – original draft, Validation, Supervision, Methodology, Funding acquisition, Conceptualization. **You Sub Kim:** Writing – original draft, Investigation, Formal analysis. **Mao-Yuan Luo:** Investigation, Formal analysis.

Declaration of Competing Interest

The authors declare that they have no known competing financial interests or personal relationships that could have appeared to influence the work reported in this paper

Data Availability

Data will be made available on request.

Acknowledgements

The present work was supported by a National Research Foundation (NRF) grant funded by the Korean government (RS-2024-00398068, 2023R1A2C2007190, RS-2023-00281671). The work at Korea Atomic Energy Research Institute (KAERI) was funded by the Internal R&D program supported by the Ministry of Science and Information Communication Technology (ICT) of the Republic of Korea (524210-22). YSN was financially supported by the Nano & Material Technology Development Program through the NRF of Korea funded by Ministry of Science and ICT (RS-2003-00281246). A portion of the current research used resources at the Spallation Neutron Source, a DOE Office of Science User Facility operated by the Oak Ridge National Laboratory (IPTS-26479 and IPTS-29338). PKL appreciates the support from (1) the National Science Foundation (DMR-1611180, 1809640, and 2226508) and (2) the US Army Research Office (W911NF-13-1-0438, W911NF-19-2-0049, and FA9550-23-1-0503). EWH appreciates the National Science and Technology Council (NSTC), Taiwan, for the financial support through Grant No. NSTC 112-2811-E-A49-521, NSTC 112-2221-E-A49-027, NSTC 113-2221-E-A49-003, and NSTC 113-2811-E-A49-525, and the travel support from the National Synchrotron Radiation Research Center (NSRRC)-Neutron Travel Program. The authors sincerely appreciate the help from the High Entropy Materials Center of the National Tsing Hua University from The Featured Areas Research Center Program within the framework of the Higher Education Sprout Project by the Ministry of Education (MOE) in Taiwan for their support.

Appendix A. Supporting information

Supplementary data associated with this article can be found in the online version at doi:10.1016/j.addma.2024.104332.

References

[1] L. Kang, H. Ge, Predicting ductile crack initiation of steel bridge structures due to extremely low-cycle fatigue using local and non-local models, J. Earthq. Eng. 17 (2013) 323–349, https://doi.org/10.1080/13632469.2012.746211.
[2] R. Liu, Z.J. Zhang, P. Zhang, Z.F. Zhang, Extremely-low-cycle fatigue behaviors of Cu and Cu-Al alloys: damage mechanisms and life prediction, Acta Mater. 83 (2015) 341–356, https://doi.org/10.1016/j.actamat.2014.10.002.
[3] B. Gludovatz, A. Hohenwarter, D. Catoor, E.H. Chang, E.P. George, R.O. Ritchie, A fracture-resistant high-entropy alloy for cryogenic applications, Science 345 (80-.) (2014) 1153–1158, https://doi.org/10.1126/science.1254581.
[4] G. Laplanche, A. Kostka, O.M. Horst, G. Eggeler, E.P. George, Microstructure evolution and critical stress for twinning in the CrMnFeCoNi high-entropy alloy, Acta Mater. 118 (2016) 152–163, https://doi.org/10.1016/j.actamat.2016.07.038.
[5] Y. Wang, B. Liu, K. Yan, M. Wang, S. Kabra, Y.L. Chiu, D. Dye, P.D. Lee, Y. Liu, B. Cai, Probing deformation mechanisms of a FeCoCrNi high-entropy alloy at 293 and 77 K using in situ neutron diffraction, Acta Mater. 154 (2018) 79–89, https://doi.org/10.1016/j.actamat.2018.05.013.
[6] H. Huang, X. Li, Z. Dong, W. Li, S. Huang, D. Meng, X. Lai, T. Liu, S. Zhu, L. Vitos, Critical stress for twinning nucleation in CrCoNi-based medium and high entropy alloys, Acta Mater. 149 (2018) 388–396, https://doi.org/10.1016/j.actamat.2018.02.037.
[7] Y.S. Kim, H. Chae, W. Woo, D.K. Kim, D.H. Lee, S. Harjo, T. Kawasaki, S.Y. Lee, Multiple deformation scheme in direct energy deposited CoCrNi medium entropy alloy at 210K, Mater. Sci. Eng. A 828 (2021) 142059, https://doi.org/10.1016/j.msea.2021.142059.
[8] W. Woo, Y.S. Kim, H.B. Chae, S.Y. Lee, J.S. Jeong, C.M. Lee, J.W. Won, Y.S. Na, T. Kawasaki, S. Harjo, K. An, Competitive strengthening between dislocation slip and twinning in cast-wrought and additively manufactured CrCoNi medium entropy alloys, Acta Mater. 246 (2023), https://doi.org/10.1016/j.actamat.2023.118699.
[9] Z. Li, K.G. Pradeep, Y. Deng, D. Raabe, C.C. Tasan, Metastable high-entropy dual-phase alloys overcome the strength-ductility trade-off, Nature 534 (2016), https://doi.org/10.1038/nature17981.
[10] M.J. Sohrabi, A. Kalhor, H. Mirzadeh, K. Rodak, H.S. Kim, Tailoring the strengthening mechanisms of high-entropy alloys toward excellent strength-ductility synergy by metalloid silicon alloying: a review, Prog. Mater. Sci. 144 (2024) 101295, https://doi.org/10.1016/j.pmatsci.2024.101295.
[11] K.Y. Tsai, M.H. Tsai, J.W. Yeh, Sluggish diffusion in Co-Cr-Fe-Mn-Ni high-entropy alloys, Acta Mater. 61 (2013) 4887–4897, https://doi.org/10.1016/j.actamat.2013.04.058.
[12] J. Dąbrowa, M. Danielewski, State-of-the-art diffusion studies in the high entropy alloys, Metals 10 (2020), https://doi.org/10.3390/met10030347.
[13] B.X. Cao, C. Wang, T. Yang, C.T. Liu, Cocktail effects in understanding the stability and properties of face-centered-cubic high-entropy alloys at ambient and cryogenic temperatures, Scr. Mater. 187 (2020) 250–255, https://doi.org/10.1016/j.scriptamat.2020.06.008.
[14] E.W. Huang, H.S. Chou, K.N. Tu, W.S. Hung, T.N. Lam, C.W. Tsai, C.Y. Chiang, B. H. Lin, A.C. Yeh, S.H. Chang, Y.J. Chang, J.J. Yang, X.Y. Li, C.S. Ku, K. An, Y. W. Chang, Y.L. Jao, Element effects on high-entropy alloy vacancy and heterogeneous lattice distortion subjected to Quasi-equilibrium heating, Sci. Rep. 9 (2019) 1–10, https://doi.org/10.1038/s41598-019-51297-4.
[15] C. Lee, G. Song, M.C. Gao, R. Feng, P. Chen, J. Brechtl, Y. Chen, K. An, W. Guo, J. D. Poplawsky, S. Li, A.T. Samaei, W. Chen, A. Hu, H. Choo, P.K. Liaw, Lattice distortion in a strong and ductile refractory high-entropy alloy, Acta Mater. 160 (2018) 158–172, https://doi.org/10.1016/j.actamat.2018.08.053.
[16] Y. Tong, S. Zhao, K. Jin, H. Bei, J.Y.P. Ko, Y. Zhang, F.X. Zhang, A comparison study of local lattice distortion in Ni80Pd20 binary alloy and FeCoNiCrPd high-

entropy alloy, Scr. Mater. 156 (2018) 14–18, https://doi.org/10.1016/j.scriptamat.2018.07.002.
[17] Z. Fu, L. Jiang, J.L. Wardini, B.E. MacDonald, H. Wen, W. Xiong, D. Zhang, Y. Zhou, T.J. Rupert, W. Chen, E.J. Lavernia, A high-entropy alloy with hierarchical nanoprecipitates and ultrahigh strength, Sci. Adv. 4 (2018) 1–9, https://doi.org/10.1126/sciadv.aat8712.
[18] L. Liu, Y. Zhang, J. Han, X. Wang, W. Jiang, C.T. Liu, Z. Zhang, P.K. Liaw, Nanoprecipitate-strengthened high-entropy alloys, Adv. Sci. 8 (2021) 1–20, https://doi.org/10.1002/advs.202100870.
[19] Y.J. Liang, L. Wang, Y. Wen, B. Cheng, Q. Wu, T. Cao, Q. Xiao, Y. Xue, G. Sha, Y. Wang, Y. Ren, X. Li, L. Wang, F. Wang, H. Cai, High-content ductile coherent nanoprecipitates achieve ultrastrong high-entropy alloys, Nat. Commun. 9 (2018) 1–8, https://doi.org/10.1038/s41467-018-06600-8.
[20] R. Feng, Y. Rao, C. Liu, X. Xie, D. Yu, Y. Chen, M. Ghazisaeidi, T. Ungar, H. Wang, K. An, P.K. Liaw, Enhancing fatigue life by ductile-transformable multicomponent B2 precipitates in a high-entropy alloy, Nat. Commun. 12 (2021) 1–10, https://doi.org/10.1038/s41467-021-23689-6.
[21] X. Chen, Q. Wang, Z. Cheng, M. Zhu, H. Zhou, P. Jiang, L. Zhou, Q. Xue, F. Yuan, J. Zhu, X. Wu, E. Ma, Direct observation of chemical short-range order in a medium-entropy alloy, Nature 592 (2021) 712–716, https://doi.org/10.1038/s41586-021-03428-z.
[22] R. Zhang, S. Zhao, J. Ding, Y. Chong, T. Jia, C. Ophus, M. Asta, R.O. Ritchie, A. M. Minor, Short-range order and its impact on the CrCoNi medium-entropy alloy, Nature 581 (2020) 283–287, https://doi.org/10.1038/s41586-020-2275-z.
[23] S. Chen, Z.H. Aitken, S. Pattamatta, Z. Wu, Z.G. Yu, D.J. Srolovitz, P.K. Liaw, Y. W. Zhang, Simultaneously enhancing the ultimate strength and ductility of high-entropy alloys via short-range ordering, Nat. Commun. 12 (2021) 1–11, https://doi.org/10.1038/s41467-021-25264-5.
[24] Z. Lei, X. Liu, Y. Wu, H. Wang, S. Jiang, S. Wang, X. Hui, Y. Wu, B. Gault, P. Kontis, D. Raabe, L. Gu, Q. Zhang, H. Chen, H. Wang, J. Liu, K. An, Q. Zeng, T.G. Nieh, Z. Lu, Enhanced strength and ductility in a high-entropy alloy via ordered oxygen complexes, Nature 563 (2018) 546–550, https://doi.org/10.1038/s41586-018-0685-y.
[25] T.Z. Khan, T. Kirk, G. Vazquez, P. Singh, A.V. Smirnov, D.D. Johnson, K. Youssef, R. Arróyave, Towards stacking fault energy engineering in FCC high entropy alloys, Acta Mater. 224 (2022) 117472, https://doi.org/10.1016/j.actamat.2021.117472.
[26] N.L. Okamoto, S. Fujimoto, Y. Kambara, M. Kawamura, Z.M.T. Chen, H. Matsunoshita, K. Tanaka, H. Inui, E.P. George, Size effect, critical resolved shear stress, stacking fault energy, and solid solution strengthening in the CrMnFeCoNi high-entropy alloy, Sci. Rep. 6 (2016) 1–10, https://doi.org/10.1038/srep35863.
[27] J. Ding, Q. Yu, M. Asta, R.O. Ritchie, Tunable stacking fault energies by tailoring local chemical order in CrCoNi medium-entropy alloys, Proc. Natl. Acad. Sci. U. S. A. 115 (2018) 8919–8924, https://doi.org/10.1073/pnas.1808660115.
[28] S. Zhao, G.M. Stocks, Y. Zhang, Stacking fault energies of face-centered cubic concentrated solid solution alloys, Acta Mater. 134 (2017) 334–345, https://doi.org/10.1016/j.actamat.2017.05.001.
[29] K. Lu, A. Chauhan, A.S. Tirunilai, J. Freudenberger, A. Kauffmann, M. Heilmaier, J. Aktaa, Deformation mechanisms of CoCrFeMnNi high-entropy alloy under low-cycle-fatigue loading, Acta Mater. 215 (2021) 117089, https://doi.org/10.1016/j.actamat.2021.117089.
[30] M.Y. Luo, T.N. Lam, P.Te Wang, N.T. Tsou, Y.J. Chang, R. Feng, T. Kawasaki, S. Harjo, P.K. Liaw, A.C. Yeh, S.Y. Lee, J. Jain, E.W. Huang, Grain-size-dependent microstructure effects on cyclic deformation mechanisms in CoCrFeMnNi high-entropy-alloys, Scr. Mater. 210 (2022) 114459, https://doi.org/10.1016/j.scriptamat.2021.114459.
[31] S. Shukla, T. Wang, S. Cotton, R.S. Mishra, Hierarchical microstructure for improved fatigue properties in a eutectic high entropy alloy, Scr. Mater. 156 (2018) 105–109, https://doi.org/10.1016/j.scriptamat.2018.07.022.
[32] S. Picak, T. Wegener, S.V. Sajadifar, C. Sobrero, J. Richter, H. Kim, T. Niendorf, I. Karaman, On the low cycle fatigue response of CoCrNiFeMn high entropy alloy with ultra-fine grain structure, Acta Mater. 205 (2021) 116540, https://doi.org/10.1016/j.actamat.2020.116540.
[33] S.A.A. Shams, G. Jang, J.W. Won, J.W. Bae, H. Jin, H.S. Kim, C.S. Lee, Low-cycle fatigue properties of CoCrFeMnNi high-entropy alloy compared with its conventional counterparts, Mater. Sci. Eng. A 792 (2020) 139661, https://doi.org/10.1016/j.msea.2020.139661.
[34] C. Peiyong, L.E.E. Chanho, W. Shao-yu, S. Mohsen, L.J.J. D.K. A, J.I.A. Haoling, X.I. E. Xie, C. Bilin, Y.E.H. Jien-wei, T. Che-wei, Y. Tao, L.P. K, , Fatigue behavior of high-entropy alloys: a review, Sci. China Technol. Sci. 61 (2018) 168–178.
[35] K. Lu, A. Chauhan, M. Walter, A.S. Tirunilai, M. Schneider, G. Laplanche, J. Freudenberger, A. Kauffmann, M. Heilmaier, J. Aktaa, Superior low-cycle fatigue properties of CoCrNi compared to CoCrFeMnNi, Scr. Mater. 194 (2021) 113667, https://doi.org/10.1016/j.scriptamat.2020.113667.
[36] J. Ren, Y. Zhang, D. Zhao, Y. Chen, S. Guan, Y. Liu, L. Liu, S. Peng, F. Kong, J. D. Poplawsky, G. Gao, T. Voisin, K. An, Y.M. Wang, K.Y. Xie, T. Zhu, W. Chen, Strong yet ductile nanolamellar high-entropy alloys by additive manufacturing, Nature 608 (2022) 62–68, https://doi.org/10.1038/s41586-022-04914-8.
[37] D. Herzog, V. Seyda, E. Wycisk, C. Emmelmann, Additive manufacturing of metals, Acta Mater. 117 (2016) 371–392, https://doi.org/10.1016/j.actamat.2016.07.019.
[38] T.H. Becker, P. Kumar, U. Ramamurty, Fracture and fatigue in additively manufactured metals, Acta Mater. 219 (2021) 117240, https://doi.org/10.1016/j.actamat.2021.117240.
[39] M.S. Pham, B. Dovgyy, P.A. Hooper, Twinning induced plasticity in austenitic stainless steel 316L made by additive manufacturing, Mater. Sci. Eng. A 704 (2017) 102–111, https://doi.org/10.1016/j.msea.2017.07.082.
[40] H. Chae, E.W. Huang, J. Jain, H. Wang, W. Woo, S.W. Chen, S. Harjo, T. Kawasaki, S.Y. Lee, Plastic anisotropy and deformation-induced phase transformation of additive manufactured stainless steel, Mater. Sci. Eng. A 762 (2019) 138065, https://doi.org/10.1016/j.msea.2019.138065.
[41] A. Yadollahi, N. Shamsaei, S.M. Thompson, D.W. Seely, Effects of process time interval and heat treatment on the mechanical and microstructural properties of direct laser deposited 316L stainless steel, Mater. Sci. Eng. A 644 (2015) 171–183, https://doi.org/10.1016/j.msea.2015.07.056.
[42] Y.J. Yin, J.Q. Sun, J. Guo, X.F. Kan, D.C. Yang, Mechanism of high yield strength and yield ratio of 316 L stainless steel by additive manufacturing, Mater. Sci. Eng. A 744 (2019) 773–777, https://doi.org/10.1016/j.msea.2018.12.092.
[43] Y.M. Wang, T. Voisin, J.T. McKeown, J. Ye, N.P. Calta, Z. Li, Z. Zeng, Y. Zhang, W. Chen, T.T. Roehling, R.T. Ott, M.K. Santala, P.J. Depond, M.J. Matthews, A. V. Hamza, T. Zhu, Additively manufactured hierarchical stainless steels with high strength and ductility, Nat. Mater. 17 (2018) 63–70, https://doi.org/10.1038/NMAT5021.
[44] Z.G. Zhu, Q.B. Nguyen, F.L. Ng, X.H. An, X.Z. Liao, P.K. Liaw, S.M.L. Nai, J. Wei, Hierarchical microstructure and strengthening mechanisms of a CoCrFeNiMn high entropy alloy additively manufactured by selective laser melting, Scr. Mater. 154 (2018) 20–24, https://doi.org/10.1016/j.scriptamat.2018.05.015.
[45] J. Wei, X.H. An, W.J. Lu, Z.M. Li, F.L. Ng, X.Z. Liao, U. Ramamurty, Selective laser melting enabling the hierarchically heterogeneous microstructure and excellent mechanical properties in an interstitial solute strengthened high entropy alloy, Mater. Rese. Lett. 3831 (2019), https://doi.org/10.1080/21663831.2019.1650131.
[46] R. Zhou, Y. Liu, C. Zhou, S. Li, W. Wu, M. Song, B. Liu, X. Liang, P.K. Liaw, Microstructures and mechanical properties of C-containing FeCoCrNi high-entropy alloy fabricated by selective laser melting, Intermetallics 94 (2018) 165–171, https://doi.org/10.1016/j.intermet.2018.01.002.
[47] R. Li, P. Niu, T. Yuan, P. Cao, C. Chen, K. Zhou, Selective laser melting of an equiatomic CoCrFeMnNi high-entropy alloy: processability, non-equilibrium microstructure and mechanical property, J. Alloy. Compd. 746 (2018) 125–134, https://doi.org/10.1016/j.jallcom.2018.02.298.
[48] T. Fujieda, H. Shiratori, K. Kuwabara, T. Kato, K. Yamanaka, Y. Koizumi, A. Chiba, First demonstration of promising selective electron beam melting method for utilizing high-entropy alloys as engineering materials, Mater. Lett. 159 (2015) 12–15, https://doi.org/10.1016/j.matlet.2015.06.046.
[49] C. Han, Q. Fang, Y. Shi, S.B. Tor, C.K. Chua, K. Zhou, Recent advances on high-entropy alloys for 3D printing, Adv. Mater. 32 (2020) 1–41, https://doi.org/10.1002/adma.201903855.
[50] Z. Qu, Z.J. Zhang, Y.K. Zhu, R. Liu, S.L. Lu, S.J. Li, Q.Q. Duan, B.N. Zhang, M. X. Zhao, J. Eckert, Z.F. Zhang, Coupling effects of microstructure and defects on the fatigue properties of laser powder bed fusion Ti-6Al-4V, Addit. Manuf. 61 (2023), https://doi.org/10.1016/j.addma.2022.103355.
[51] Z. Tong, X. Ren, J. Jiao, W. Zhou, Y. Ren, Y. Ye, E.A. Larson, J. Gu, Laser additive manufacturing of FeCrCoMnNi high-entropy alloy: effect of heat treatment on microstructure, residual stress and mechanical property, J. Alloy. Compd. 785 (2019) 1144–1159, https://doi.org/10.1016/j.jallcom.2019.01.213.
[52] W. Zhang, A. Chabok, B.J. Kooi, Y. Pei, Additive manufactured high entropy alloys: a review of the microstructure and properties, Mater. Des. 220 (2022) 110875, https://doi.org/10.1016/j.matdes.2022.110875.
[53] H. Khodashenas, H. Mirzadeh, Post-processing of additively manufactured high-entropy alloys - a review, J. Mater. Res. Technol. 21 (2022) 3795–3814, https://doi.org/10.1016/j.jmrt.2022.11.027.
[54] A. Järvenpää, L.P. Karjalainen, M. Jaskari, Effect of grain size on fatigue behavior of Type 301LN stainless steel, Int. J. Fatigue 65 (2014) 93–98, https://doi.org/10.1016/j.ijfatigue.2013.05.012.
[55] Y. Uematsu, T. Kakiuchi, H. Miura, T. Nozaki, Effect of grain size on fatigue behavior in AZ61 Mg alloys fabricated by MDFing, Mater. Trans. 57 (2016) 1454–1461, https://doi.org/10.2320/matertrans.MH201508.
[56] A. Yadollahi, N. Shamsaei, Additive manufacturing of fatigue resistant materials: challenges and opportunities, Int. J. Fatigue 98 (2017) 14–31, https://doi.org/10.1016/j.ijfatigue.2017.01.001.
[57] Z. Qu, Z. Zhang, R. Liu, L. Xu, Y. Zhang, X. Li, Z. Zhao, Q. Duan, S. Wang, S. Li, Y. Ma, X. Shao, R. Yang, J. Eckert, R.O. Ritchie, Z. Zhang, High fatigue resistance in a titanium alloy via near-void-free 3D printing, Nature 626 (2024) 999–1004, https://doi.org/10.1038/s41586-024-07048-1.
[58] S. Leuders, T. Lieneke, S. Lammers, T. Tröster, T. Niendorf, On the fatigue properties of metals manufactured by selective laser melting - the role of ductility, J. Mater. Res. 29 (2014) 1911–1919, https://doi.org/10.1557/jmr.2014.157.
[59] K. An, H.D. Skorpenske, A.D. Stoica, D. Ma, X.L. Wang, E. Cakmak, First in situ lattice strains measurements under load at VULCAN, Metall. Mater. Trans. A Phys. Metall. Mater. Sci. 42 (2011) 95–99, https://doi.org/10.1007/s11661-010-0495-9.
[60] H. Chae, E.W. Huang, J. Jain, D.H. Lee, S. Harjo, T. Kawasaki, S.Y. Lee, Mechanical stability of retained Austenite and texture evolution in additively manufactured stainless steel, Met. Mater. Int. 30 (2024) 1321–1330, https://doi.org/10.1007/s12540-023-01575-8.
[61] S.Y. Lee, H. Wang, M.A. Gharghouri, G. Nayyeri, W. Woo, E. Shin, P.D. Wu, W. J. Poole, W. Wu, K. An, Deformation behavior of solid-solution-strengthened Mg-9 wt% Al alloy: in situ neutron diffraction and elastic-viscoplastic self-consistent modeling, Acta Mater. 73 (2014) 139–148, https://doi.org/10.1016/j.actamat.2014.03.038.
[62] T. Unga, J. Gubicza, G. Riba, MWP-fit: A Program for Multiple Whole-profile Fitting of Diffraction Peak Profiles by ab initio Theoretical Functions, (2001) 669–676. https://doi.org/10.1107/S0021889801011451.

[63] T. Ungár, Microstructural parameters from X-ray diffraction peak broadening, Scr. Mater. 51 (2004) 777–781, https://doi.org/10.1016/j.scriptamat.2004.05.007.
[64] L. Balogh, Stacking fAults and Twin Boundaries in fcc Crystals Determined by x-ray Diffraction Profile Analysis □, 023512 (2006). https://doi.org/10.1063/1.2216195.
[65] B. Wang, H. He, M. Naeem, S. Lan, S. Harjo, T. Kawasaki, Y. Nie, H.W. Kui, T. Ungár, D. Ma, A.D. Stoica, Q. Li, Y. Ke, C.T. Liu, X. Wang, Deformation of CoCrFeNi high entropy alloy at large strain Macroscopic True Stress, MPa CoCrFeNi Transverse Direction, Scr. Mater. 155 (2018) 54–57, https://doi.org/10.1016/j.scriptamat.2018.06.013.
[66] J. Bertalan, The Convolutional Multiple Whole Profile (CMWP) fitting method, a global optimization procedure for microstructure determination, Crystals 10 (2020) 22–24.
[67] Y. Hu, J. Shi, X. Cao, J. Zhi, Low cycle fatigue life assessment based on the accumulated plastic strain energy density, Materials 14 (2021), https://doi.org/10.3390/ma14092372.
[68] H. Xu, D. Ye, L. Mei, A study of the back stress and the friction stress behaviors of Ti-6Al-4V alloy during low cycle fatigue at room temperature, Mater. Sci. Eng. A 700 (2017) 530–539, https://doi.org/10.1016/j.msea.2017.06.051.
[69] P. Guo, L. Qian, J. Meng, F. Zhang, L. Li, Low-cycle fatigue behavior of a high manganese austenitic twin-induced plasticity steel, Mater. Sci. Eng. A 584 (2013) 133–142, https://doi.org/10.1016/j.msea.2013.07.020.
[70] J. Jadav, K.V. Rajulapati, K.B.S. Rao, N.E. Prasad, R. Mythili, K. Prasad, Strain controlled isothermal low cycle fatigue life, deformation and fracture characteristics of Superni 263 superalloy, Mater. Sci. Eng. A 760 (2019) 296–315, https://doi.org/10.1016/j.msea.2019.05.119.
[71] M. Delbove, J.B. Vogt, J. Bouquerel, T. Soreau, F. Primaux, Low cycle fatigue behaviour of a precipitation hardened Cu-Ni-Si alloy, Int. J. Fatigue 92 (2016) 313–320, https://doi.org/10.1016/j.ijfatigue.2016.07.019.
[72] R.L. McDaniels, L. Chen, R. Steward, P.K. Liaw, R.A. Buchanan, S. White, K. Liaw, D.L. Klarstrom, The strain-controlled fatigue behavior and modeling of Haynes® HASTELLOY® C-2000® superalloy, Mater. Sci. Eng. A 528 (2011) 3952–3960, https://doi.org/10.1016/j.msea.2010.10.024.
[73] S. Mu, Y. Li, D. Song, B. Xu, X. Chen, Low cycle fatigue behavior and failure mechanism of wire arc additive manufacturing 16MND5 bainitic steel, J. Mater. Eng. Perform. 30 (2021) 4911–4924, https://doi.org/10.1007/s11665-021-05554-1.
[74] Y. Li, Y. Yuan, D. Wang, S. Fu, D. Song, M. Vedani, X. Chen, Low cycle fatigue behavior of wire arc additive manufactured and solution annealed 308 L stainless steel, Addit. Manuf. 52 (2022) 102688, https://doi.org/10.1016/j.addma.2022.102688.
[75] S.A.A. Shams, G. Kim, J.W. Won, J.N. Kim, H.S. Kim, C.S. Lee, Effect of grain size on the low-cycle fatigue behavior of carbon-containing high-entropy alloys, Mater. Sci. Eng. A 810 (2021) 140985, https://doi.org/10.1016/j.msea.2021.140985.
[76] C.W. Shao, P. Zhang, R. Liu, Z.J. Zhang, J.C. Pang, Q.Q. Duan, Z.F. Zhang, A remarkable improvement of low-cycle fatigue resistance of high-Mn austenitic TWIP alloys with similar tensile properties: importance of slip mode, Acta Mater. 118 (2016) 196–212, https://doi.org/10.1016/j.actamat.2016.07.034.
[77] T. Niendorf, T. Wegener, Z. Li, D. Raabe, Unexpected cyclic stress-strain response of dual-phase high-entropy alloys induced by partial reversibility of deformation, Scr. Mater. 143 (2018) 63–67, https://doi.org/10.1016/j.scriptamat.2017.09.013.
[78] V. Patlan, A. Vinogradov, K. Higashi, K. Kitagawa, Overview of fatigue properties of fine grain 5056 Al-Mg alloy processed by equal-channel angular pressing, Mater. Sci. Eng. A 300 (2001) 171–182, https://doi.org/10.1016/S0921-5093(00)01682-8.
[79] S.W. Wu, G. Wang, Y.D. Jia, J. Yi, Q.J. Zhai, C.T. Liu, B.A. Sun, H.J. Chu, J. Shen, P. K. Liaw, T.Y. Zhang, Enhancement of strength-ductility trade-off in a high-entropy alloy through a heterogeneous structure, Acta Mater. 165 (2019), https://doi.org/10.1016/j.actamat.2018.12.012.
[80] Q. Xie, Y. Chen, P. Yang, Z. Zhao, Y.D. Wang, K. An, In-situ neutron diffraction investigation on twinning/detwinning activities during tension-compression load reversal in a twinning induced plasticity steel, Scr. Mater. 150 (2018) 168–172, https://doi.org/10.1016/j.scriptamat.2018.03.017.
[81] W. Wu, P.K. Liaw, K. An, Unraveling cyclic deformation mechanisms of a rolled magnesium alloy using in situ neutron diffraction, Acta Mater. 85 (2015) 343–353, https://doi.org/10.1016/j.actamat.2014.11.030.
[82] T. Sawaguchi, Y. Tomota, F. Yoshinaka, S. Harjo, Evidence supporting reversible martensitic transformation under cyclic loading on Fe–Mn–Si–Al alloys using in situ neutron diffraction, Acta Mater. 242 (2023) 118494, https://doi.org/10.1016/j.actamat.2022.118494.
[83] M. Eskandari, M.A. Mohtadi-Bonab, A. Zarei-Hanzaki, A.G. Odeshi, J.A. Szpunar, High-resolution EBSD study of adiabatic shear band and neighboring grains after dynamic impact loading of Mn-steel used in vehicle structure, J. Mater. Eng. Perform. 25 (2016) 1611–1620, https://doi.org/10.1007/s11665-016-1923-9.
[84] Q. Zhu, Z. Li, S. Wei, Y. Zhao, U. Ramamurty, J. Wang, H. Gao, A deformation twin mediated sliding-opening zig-zag fracture mechanism in multi-principal element alloys, Acta Mater. 275 (2024) 120073, https://doi.org/10.1016/j.actamat.2024.120073.
[85] A.G. Wang, X.H. An, J. Gu, X.G. Wang, L.L. Li, W.L. Li, M. Song, Q.Q. Duan, Z. F. Zhang, X.Z. Liao, Effect of grain size on fatigue cracking at twin boundaries in a CoCrFeMnNi high-entropy alloy, J. Mater. Sci. Technol. 39 (2020) 1–6, https://doi.org/10.1016/j.jmst.2019.09.010.
[86] G. Laplanche, A. Kostka, C. Reinhart, J. Hunfeld, G. Eggeler, E.P. George, Reasons for the superior mechanical properties of medium-entropy CrCoNi compared to high-entropy CrMnFeCoNi, Acta Mater. 128 (2017) 292–303, https://doi.org/10.1016/j.actamat.2017.02.036.
[87] C. Somsen, H. Bei, G. Eggeler, E.P. George, The influences of temperature and microstructure on the tensile properties of a CoCrFeMnNi high-entropy alloy, Acta Mater. 61 (2013) 5743–5755, https://doi.org/10.1016/j.actamat.2013.06.018.
[88] I. Karaman, G.G. Yapici, Y.I. Chumlyakov, I.V. Kireeva, Deformation twinning in difficult-to-work alloys during severe plastic deformation, Mater. Sci. Eng. A 410–411 (2005) 243–247, https://doi.org/10.1016/j.msea.2005.08.021.
[89] X. Sun, S. Lu, R. Xie, X. An, W. Li, T. Zhang, C. Liang, X. Ding, Y. Wang, H. Zhang, L. Vitos, Can experiment determine the stacking fault energy of metastable alloys? Mater. Des. 199 (2021) https://doi.org/10.1016/j.matdes.2020.109396.
[90] S. Lu, X. Sun, Y. Tianc, X. An, W. Lia, Y. Chen, H. Zhang, L. Vitos, Theory of transformation-mediated twinning Significance Statement, PNAS Nexus 2 (2022) 1–11.
[91] Q. Zhang, R. Niu, Y. Liu, J. Jiang, F. Xu, X. Zhang, J.M. Cairney, X. An, X. Liao, H. Gao, X. Li, Room-temperature super-elongation in high-entropy alloy nanopillars, Nat. Commun. 14 (2023) 1–10, https://doi.org/10.1038/s41467-023-42894-z.
[92] H. Suzuki, Segregation of solute atoms to stacking faults, J. Phys. Soc. Jpn. 17 (1962) 322–325, https://doi.org/10.1143/JPSJ.17.322.
[93] C.C. Wang, J.H. Chen, J.W. Yeh, S.J. Lin, S.Y. Chang, Y.C. Lo, C.C. Yen, K.H. Lin, C. M. Tseng, T.N. Lam, S.A. Chen, C.S. Wu, C.K. Chang, B.H. Lin, M.T. Tang, H. S. Sheu, S.W. Chen, E.W. Huang, Microstructure evolution in high-pressure phase transformations of CrFeNi and CoCrFeMnNi alloys, J. Alloy. Compd. 918 (2022) 165383, https://doi.org/10.1016/j.jallcom.2022.165383.
[94] P.P. Bhattacharjee, G.D. Sathiaraj, M. Zaid, J.R. Gatti, C. Lee, C.W. Tsai, J.W. Yeh, Microstructure and texture evolution during annealing of equiatomic CoCrFeMnNi high-entropy alloy, J. Alloy. Compd. 587 (2014) 544–552, https://doi.org/10.1016/j.jallcom.2013.10.237.
[95] S.Y. Lee, P.K. Liaw, H. Choo, R.B. Rogge, A study on fatigue crack growth behavior subjected to a single tensile overload: Part I. An overload-induced transient crack growth micromechanism, Acta Mater. 59 (2011) 485–494, https://doi.org/10.1016/j.actamat.2010.09.049.